Weakening of Antarctic Stratospheric Planetary Wave Activities in Early Austral Spring Since the Early 2000s: A Response to Sea Surface Temperature Trends

YIHANG HU, WENSHOU TIAN, JIANKAI ZHANG, TAO WANG, MIAN XU

Key Laboratory for Semi-Arid Climate Change of the Ministry of Education, College of Atmospheric Sciences, Lanzhou University, China

*Correspondence to: wstian@lzu.edu.cn

Abstract

Using multiple reanalysis datasets and modeling simulations, the trends of Antarctic stratospheric planetary wave activities in early austral spring since the early 2000s are investigated in this study. We find that the stratospheric planetary wave activities in September have weakened significantly since 2000, which is mainly related to the weakening of the tropospheric wave sources in the extratropical southern hemisphere. As the Antarctic ozone also shows clear shift around 2000, the impact of ozone recovery on Antarctic planetary wave activity is also examined through numerical simulations. Significant ozone recovery in lower stratosphere changes the atmospheric state for wave propagation to some extent, inducing a slight decrease of vertical wave flux in upper troposphere and lower stratosphere (UTLS). However, the changes of wave propagation environment in middle and upper stratosphere over subpolar region are not significant. The ozone recovery has minor contribution to the significant weakening of stratospheric planetary wave activity in September. Further analysis indicates that the trend of September sea surface temperature (SST) over 20° N-70°S is well linked to the weakening of stratospheric planetary wave activities. The model simulations reveal that the SST trend in the extratropical southern hemisphere (20°S-70°S) and the tropics (20°N-20°S) induce a weakening of wave-1 component of tropospheric geopotential height in the extratropical southern hemisphere, which subsequently leads to a decrease in stratospheric wave flux. In addition, both reanalysis data and numerical simulations indicate that the Brewer-Dobson circulation (BDC) related to wave activities in the stratosphere has also been weakening in early austral

spring since 2000 due to the trend of September SST in the tropics and extratropical southern hemisphere.

Key words: *Antarctic; Stratospheric planetary wave activities; Tropospheric wave sources; Sea surface temperature*

1. Introduction

The stratospheric planetary wave activities have important influences on stratospheric temperature (e.g., Hu & Fu, 2009; Lin et al., 2009; Li & Tian, 2017; Li et al., 2018), polar vortex (e.g., Kim et al., 2014; Zhang et al., 2016; Hu et al., 2018) and distribution of chemical substances (e.g., Gabriel et al., 2011; Ialongo et al., 2012; Kravchenko et al., 2011; Zhang et al., 2019a). Meanwhile, the stratospheric circulation modulated by planetary waves can exert impacts on tropospheric weather and climate (e.g., Haigh et al., 2005; Zhang et al., 2019b) through downward control processes (Haynes et al., 1991), which is useful for extended forecast by using preceding signals in the stratosphere (e.g., Baldwin et al., 2001; Wang et al., 2020).

The planetary perturbations generated by large-scale topography, convection and continent-ocean heating contrast can propagate from the troposphere to the stratosphere (Charney & Drazin, 1961) and form stratospheric planetary waves. As the land-sea thermal contrast in the northern hemisphere is larger than that in the southern hemisphere and produces stronger zonal forcing for the genesis of stratospheric waves, the majority of attention has been given to wave activities and their impacts on weather

and climate in the northern hemisphere (e.g., Kim et al., 2014; Zhang et al., 2016; Hu et al., 2018). However, planetary wave activities in the southern hemisphere also play an important role in heating the stratosphere dynamically (e.g., Hu & Fu, 2009; Lin et al., 2009), which suppresses Polar Stratospheric Clouds (PSCs) formation and ozone depletion (e.g., Shen et al., 2020a; Tian et al., 2017). The Antarctic sudden stratospheric warming (SSW) that occurred in 2002 (e.g., Baldwin et al., 2003; Nishii & Nakamura, 2004; Newman & Nash, 2005) and 2019 (e.g., Yamazaki el al., 2020; Shen et al., 2020a; Shen et al., 2020b) was associated with significant upward propagation of wave flux. Such episodes are extraordinarily rare in the history, and the one in 2019 contributed to the formation of the smallest Antarctic ozone hole on record (WMO, 2019). In addition, some studies reported that wildfires in Australia at the end of 2019 are related to negative phase of the Southern Annular Mode (SAM), which was induced by the extended influence of the SSW event that occurred in September (Lim et al., 2019; Shen et al., 2020b). In a word, the Antarctic planetary wave activities are important for the stratosphere-troposphere interactions and climate system in the southern hemisphere.

Long-term observations in the Antarctic stratosphere show a significant ozone decline from the early 1980s to the early 2000s due to anthropogenic emission of chlorofluorocarbons (CFCs) (WMO, 2011) and a recovery signal since 2000s because of phasing out CFCs in response to Montreal Protocol (e.g., Angell and Free, 2009; Krzyścin, 2012; Zhang et al., 2014; Banerjee et al., 2020). The Antarctic stratospheric ozone depletion and recovery have important impacts on climate in the southern hemisphere. The ozone depletion cools the Antarctic stratosphere through reducing

absorption of radiation and leads to the strengthening of Antarctic polar vortex during austral spring (e.g., Randel & Wu, 1999; Solomon, 1999; Thompson et al., 2011). The anomalous circulation in the Antarctic stratosphere during austral spring exerts impacts on tropospheric circulations (e.g., intensification of SAM index, poleward shift of tropospheric jet position and expansion of the Hadley cell edge) in the subsequent months (e.g., Thompson et al., 2011; Swart & Fyfe, 2012; Son et al., 2018; Banerjee et al., 2020) and influences the distribution of precipitation and dry zone in the southern hemisphere (e.g., Thompson et al., 2011; Barnes et al., 2013; Kang et al., 2011). Following the healing of ozone loss in the Antarctic ozone hole since 2000s (e.g., Solomon et al., 2016; Susan et al., 2019), great attention has been paid on possible impacts of ozone recovery on climate system in the southern hemisphere (e.g., Son et al., 2008; Barnes et al., 2013; Xia et al., 2020; Banerjee et al., 2020). Son et al. (2008) implemented the Chemistry-Climate Model Validation (CCMVal) models to predict the response of the southern hemisphere westerly jet to stratospheric ozone recovery. Based on the Phase 5 of Coupled Model Intercomparison Projects (CMIP5) models, Barnes et al. (2013) proposed that the tropospheric jet and dry zone edge no longer shift poleward during austral summer since the early 2000s due to ozone recovery. Banerjee et al. (2020) analyzed observations and reanalysis datasets. They found that following the ozone recovery after 2000, the increase of SAM index and the poleward shifting of tropospheric jet position as well as the Hadley cell edge all experienced a pause. Their results suggest that ozone depletion and recovery have made important contributions to the climate shift that occurred around 2000 in the southern hemisphere.

However, some previous studies have reported zonally asymmetric warming patterns in Antarctic stratosphere, which are generated by increased planetary wave activities during austral spring from the early 1980s to the early 2000s (Hu & Fu, 2009; Lin et al., 2009). Note that the Antarctic stratosphere was experiencing radiative cooling in the same period due to ozone depletion (e.g., Randel & Wu, 1999; Solomon, 1999; Thompson et al., 2011). The increase in stratospheric planetary wave activities cannot be explained by ozone decline, because the acceleration of stratospheric circumpolar wind caused by radiative cooling induces more wave energy to be reflected back to the troposphere (e.g., Andrews et al., 1987; Holton et al., 2004). Hu & Fu (2009) attributed the increase in Antarctic stratospheric wave activities to the SST trend from the 1980s to the 2000s. Their results indicate that in addition to ozone change, other factors such as changes in SST also contribute to climate change in the southern hemisphere. Moreover, the phase of Interdecadal Pacific Oscillation (IPO) also changed at around 2000 (e.g., Trenberth et al., 2013). SST variation influences Rossby wave propagation and tropospheric wave sources, and thereby indirectly affects stratospheric wave activities (e.g., Lin et al., 2012; Hu et al., 2018; Tian et al., 2017). The questions here are: (1) Has the trend of stratospheric planetary wave activity in the southern hemisphere been shifting since the 2000s? (2) What are the factors responsible for the trend of Antarctic stratospheric planetary wave activity since the 2000s?

In this study, we reveal the trend of Antarctic planetary wave activity in early austral spring since the 2000s based on multiple reanalysis datasets. We also conduct

sensitive experiments forced by linear increments of ozone and SST fields since the 2000s to investigate the response of Antarctic planetary activity to above two factors. The remainder of the paper is organized as follows. Section 2 describes the data, methods and configurations of model simulations. Section 3 presents the trends of stratospheric and tropospheric wave activities in early austral spring. Section 4 examines the impact of ozone recovery on Antarctic stratospheric planetary wave activity. Section 5 investigates the connections between the trends of SST and stratospheric wave activities. Sections 6 discusses the responses of tropospheric wave sources and stratospheric wave activities to SST changes based on model simulations. Major conclusions and discussion are presented in Section 7.

2. Datasets, methods and experimental configurations

a. Datasets

In this study, daily and monthly mean data extracted from the Modern-Era Retrospective analysis for Research and Applications Version 2 (MERRA-2; Bosilovich et al., 2015) dataset are used to calculate trends of Brewer-Dobson circulation (BDC), tropospheric wave sources, and the Elisassen-Palm (E-P) flux and its divergence in September. To verify the trend of stratospheric E-P flux, we also refer to the results derived from the European Centre for Medium-range Weather Forecasting (ECMWF) Interim Reanalysis (ERA-Interim; Dee et al., 2011) dataset, the Japanese 55-year Reanalysis (JRA-55; Kobayashi et al., 2015) dataset and the National Centers for Environmental Prediction-Department of Energy Global Reanalysis 2 (NCEP-2; Kanamitsu et al., 2002) dataset.

The observed total column ozone (TCO) data are extracted from SBUV v8.6 satellite dataset, which is a monthly and zonal mean dataset on 5° grid. Ozone data derived from MERRA-2 dataset are also used to calculate TCO.

SST data are extracted from the Extended Reconstructed Sea Surface Temperature (ERSST) dataset, which is a global monthly mean sea surface temperature dataset derived from the International Comprehensive Ocean-Atmosphere Dataset (ICOADS). The ERSST is on global 2°×2° grid and covers the period from January 1854 to the present. We use the latest version (version 5, i.e., v5) dataset to calculate trends and correlations, and produce SST forcing field for model simulations. More details about this version of ERSST can be found in Huang et al. (2017).

In addition, the unfiltered Interdecadal Pacific Oscillation (IPO) index derived from the ERSST v5 dataset is also used in this study. More detailed information about the index can be found in Henley et al. (2015).

b. Diagnosis of wave activities and Brewer-Dobson circulation

Planetary wave activities are measured by E-P flux ($\vec{F} \equiv (0, F^{(\phi)}, F^{(z)})$) and its divergence D_F. Their algorithms are expressed by Eqs. (1)-(3) (Andrews et al., 1987):

$$F^{(\phi)} = \rho_0 a \cos\phi (\overline{u}_z \overline{v'\theta'} / \overline{\theta}_z - \overline{v'u'}) \tag{1}$$

$$F^{(z)} = \rho_0 a \cos\phi \{ [f - (a\cos\phi)^{-1} (\overline{u}\cos\phi)_\phi] \overline{v'\theta'} / \overline{\theta}_z - \overline{w'u'} \} \tag{2}$$

$$D_F = \frac{\nabla \cdot \vec{F}}{\rho_0 a \cos\phi} = \frac{(a\cos\phi)^{-1} \frac{\partial}{\partial \phi} (F^{(\phi)} \cos\phi) + \frac{\partial F^{(z)}}{\partial z}}{\rho_0 a \cos\phi} \tag{3}$$

where u, v represent zonal and meridional components of horizontal wind, w is vertical velocity, θ is potential temperature, a is the Earth radius, f is the

Coriolis parameter, z is geopotential height, ϕ is latitude, ρ_0 is the background air density.

The quasi-geostrophic refractive index (RI) is used to diagnose the environment of wave propagation (Chen & Robinson, 1992). Its algorithm is written as Eq. (4):

$$RI = \frac{\bar{q}_\varphi}{\bar{u}} - (\frac{k}{a\cos\varphi})^2 - (\frac{f}{2NH})^2 \tag{4}$$

where the zonal-mean potential vorticity meridional gradient $\bar{q}_\varphi$ is

$$\bar{q}_\varphi = \frac{2\Omega}{a}\cos\varphi - \frac{1}{a^2}[\frac{(\bar{u}\cos\varphi)_\varphi}{a\cos\varphi}]_\varphi - \frac{f^2}{\rho_0}(\rho_0\frac{\bar{u}_z}{N^2})_z \tag{5}$$

H, q, k, N^2 and Ω are the scale height, potential vorticity, zonal wave number, buoyancy frequency, and Earth's angular frequency, respectively.

The Brewer-Dobson circulation driven by wave breaking in the stratosphere is closely related to stratospheric wave activities. Its meridional and vertical components $(\bar{v}^*, \bar{w}^*)$ and stream function ($\psi^*(p,\phi)$) are expressed by Eqs. (4)-(6) (Andrews et al., 1987; Birner & Bönisch, 2011) :

$$\bar{v}^* \equiv \bar{v} - \rho_0^{-1}(\rho_0\overline{v'\theta'}/\bar{\theta}_z)_z \tag{6}$$

$$\bar{w}^* \equiv \bar{w} + (a\cos\phi)^{-1}(\cos\phi\cdot\overline{v'\theta'}/\bar{\theta}_z)_\phi \tag{7}$$

$$\psi^*(p,\phi) = \int_0^p \frac{-2\pi a\cdot\cos\phi\cdot\bar{v}^*(p'',\phi)}{g}dp'' \tag{8}$$

where p is the air pressure, π is the circular constant, g is the gravitational acceleration.

In Eqs. (1)-(8), the overbar and prime denote a zonal mean and departure from the zonal mean, respectively. The subscripts denote partial derivatives. The Fourier decomposition is used to obtain components of Eqs. (1)-(3) with different zonal wave

numbers. Meanwhile, the Fourier decomposed components of geopotential height zonal deviations are also used to determine tropospheric wave sources.

c. Statistical methods

The trend is measured by the slope of linear regression based on the least square estimation. The correlation is used to analyze statistical links between different variables. In this paper, all the time series have been linearly detrended before calculating correlation coefficients (r) and their corresponding significances.

The change-point testing (e.g. Banerjee et al., 2020) is used to make sure the significance of trend or correlation coefficient is not unduly influenced by some particular beginning or ending years, and thereby confirm that the trend exists objectively.

We use two-tailed student's t test to calculate the significances of trend, correlation coefficient or mean difference. The result of significance test is measured by p value or confidence intervals in this paper. $p \le 0.1$, $p \le 0.05$ and $p \le 0.01$ suggest the trend, correlation coefficient or mean difference is significant at/above the 90%, 95% and 99% confidence levels, respectively. The confidence interval of trend is shown in (7) (Shirley et al., 2004):

$$[\hat{b} - t_{1-\alpha/2}(n-2)\hat{\sigma}_b, \hat{b} + t_{1-\alpha/2}(n-2)\hat{\sigma}_b] \quad (7)$$

where $\hat{b}$ is estimated value of slope, $\hat{\sigma}_b$ is standard error of slope and it is written as: $\hat{\sigma}_b = \hat{b} \cdot \sqrt{\frac{\frac{1}{r^2} - 1}{n-2}}$, $t_{1-\alpha/2}(n-2)$ denotes the value of t-distribution with the degree of freedom equal to $n-2$ and the two-tailed confidence level equal to $1-\alpha$ ($\alpha = 0.90$,

196 0.95 or 0.99). The confidence interval of mean difference is expressed by Eq. (8)
197 (Shirley et al., 2004):

198 $$[\bar{X}-\bar{Y}-t_{1-\alpha/2}(M+N-2)\cdot S_w\cdot\sqrt{\frac{1}{M}+\frac{1}{N}},\ \bar{X}-\bar{Y}+t_{1-\alpha/2}(M+N-2)\cdot S_w\cdot\sqrt{\frac{1}{M}+\frac{1}{N}}] \quad (8)$$

199 where

200 $$S_w=\sqrt{\frac{1}{M+N-2}[\sum_{i=1}^{M}(X_i-\bar{X})^2+\sum_{j=1}^{N}(Y_j-\bar{Y})^2]} \quad (9)$$

201 Here, $\bar{X}$ and $\bar{Y}$ are the sample averages, M and N are the numbers of sample
202 sizes with two populations, $t_{1-\alpha/2}(M+N-2)$ denotes the value of t-distribution with
203 the degree of freedom equal to $M+N-2$ and the two-tailed confidence level equal to
204 $1-\alpha$.

205 Previous studies have indicated that SST impact on the stratosphere shows a
206 spatial dependence (e.g., Xie et al., 2020). To find out a robust relationship between the
207 trend of SST in a specific region and the trend of stratospheric wave activities, we divide
208 the global ocean into three regions: SH (the extratropical southern hemisphere, 70°S-
209 20°S), TROP (the tropics, 20°S-20°N) and NH (the extratropical northern hemisphere,
210 20°N-70°N). Since the impacts in different regions might be combined, we also
211 consider three combined regions named as SHtrop (the extratropical southern
212 hemisphere and the tropics, 70°S-20°N), NHtrop (the extratropical northern hemisphere
213 and the tropics, 20°S-70°N) and the Globe (70°S-70°N). To find statistical connections
214 between the trend of SST and that of stratospheric wave activities, we examine the first
215 three leading patterns (EOF1, EOF2, EOF3) and principal components (PC1, PC2, PC3)
216 of SST in above six regions obtained from Empirical Orthogonal Function (EOF)

analysis. In all the six regions, there is always one EOF mode that shows great similarity to the spatial pattern of trend (not shown) as we do not detrend SST time series when the EOF analysis is carried out. Thus, the significance of the correlation between the PC time series of that EOF mode and time series of stratospheric E-P flux can be used as the criterion to determine the statistical connection between the trend of SST and the trend of stratospheric wave activities.

d. The model and experiment configurations

The F_2000_WACCM_SC (FWSC) component in the Community Earth System Model (CESM; version 1.2.0) is used to verify the impacts of SST and ozone recovery on tropospheric wave sources and stratospheric wave activities in early austral spring. The FWSC component is the Whole Atmosphere Community Climate Model version 4 (WACCM4) with specified chemistry forcing fields (such as ozone, greenhouse gases (GHG), aerosols and so on), which have fixed values in 2000 by default. The WACCM4 includes active atmosphere, data ocean (run as a prescribed component, simply reading SST forcing data instead of running ocean model), land and sea ice. Physics schemes in the WACCM4 are based on those in the Community Atmospheric Model version 4 (CAM4; Neale et al., 2013). The WACCM4 uses a finite-volume dynamic framework and extends from the ground to approximately 145 km (5.1×10^{-6} hPa) altitude in the vertical with 66 vertical levels. The simulations presented in this paper are conducted at a horizontal resolution of 1.9°×2.5°. More information about the WACCM can be found in Marsh et al. (2013).

Control experiments and sensitive experiments are conducted to investigate

responses of Antarctic stratospheric wave activities to SST trends and the ozone recovery trend in early austral spring. For the experiments of SST trends, monthly mean global SST during 1980-2000 derived from the ERSST v5 dataset is used as SST forcing field in the control experiment (sstctrl). For the four sensitive experiments (sstNH, sstSH, ssttrop, sstSHtrop), linear increments of SST in different regions in September during 2000-2017 are used as the forcing field. Ozone, aerosols and greenhouse gases (GHG) in the control experiment and the four sensitive experiments all have the fixed values in 2000. For the experiments of ozone recovery trend, monthly mean three-dimensional global ozone during 1980-2000 derived from the MERRA-2 dataset is used as the ozone forcing field in the control experiment (O3ctrl). The sensitive experiment (O3sen) is forced by linear increments of ozone in September during 2001-2017. The SSTs in O3ctrl and O3sen both are monthly mean global SST during 1980-2000. The aerosol and greenhouse gases values in 2000 are used. These experiment configurations are summarized and listed in Table 1 and Table 2.

Firstly, we run the FWSC component to generate randomly different initial conditions for 120 years with free run. Then, each experiment includes 100 ensemble members that run from July to September forced by these initial conditions from the 21st year to the 120th year in July. The forcing fields of SST and ozone are only superposed from July to September. July and August are taken as spin-up time and simulations during this period are discarded. The ensemble mean in September derived from these 100 ensemble members is regarded as the final result of each experiment. A similar approach is implemented for sensitive experiments, in which the forcing fields

superposed only in certain months. The same approach has been used in previous studies (e.g., Zhang et al., 2018).

3. Trend of planetary wave activities in early austral spring

Figure 1 shows the trends of stratospheric planetary wave activities in the southern hemisphere September during 1980-2000 and 2000-2017, respectively. Note that the vertical E-P flux entering into the stratosphere over 50°S-70°S in September has been increasing during 1980-2000, accompanied by intensified wave flux convergence in the upper stratosphere (Fig. 1a) that is mainly contributed by the wave-1 component (Fig. 1b). This feature implies that the stratospheric planetary wave activities have strengthened in early austral spring during 1980-2000. A similar result has been reported in previous studies (Hu & Fu, 2009; Lin et al., 2009). During 2000-2017, however, vertical propagation of stratospheric E-P flux weakened over the subpolar region of the southern hemisphere, which was accompanied by intensified wave flux divergence in the upper stratosphere (Fig. 1d) mainly contributed by the wave-1 component (Fig. 1e) while the wave-2 component also made certain contributions (Fig. 1f). Similar features also appear in August, but not as significant as that in September (Fig. S1). For this reason, hereafter we focus on the features in September.

The SSW that occurred in 2002 was accompanied with large upward wave fluxes in the stratosphere, which is extremely rare in history and has been studied extensively in previous studies (e.g., Baldwin et al., 2003; Nishii & Nakamura, 2004; Newman & Nash, 2005). Since the period with a negative trend of stratospheric vertical wave flux is short, it is necessary to further investigate whether such a negative trend is artificially

283 influenced by the single year of 2002. Therefore, following Banerjee et al. (2020), we
284 use a change-point method to test the significance of the trend during various periods
285 based on four reanalysis datasets (ERA-Interim, MERRA-2, JRA-55, NCEP-2).
286 Figures 2a (including the year 2002) and 2b (excluding the year 2002) display the time
287 series of area-weighted vertical stratospheric wave flux (Fz) over the southern
288 hemisphere subpolar region obtained from different reanalysis datasets. Note that the
289 wave flux time series obtained from the four reanalysis datasets all present a positive
290 trend from the early 1980s to the early 2000s and a negative trend from the early 2000s
291 to present, regardless of whether the extreme value in 2002 is removed or not. The
292 correlation coefficients of the time series between these reanalysis datasets are above
293 0.9 and statistically significant (Table 3), suggesting that the time series derived from
294 different datasets are consistent with each other. Figures 2c-f show the trends and
295 corresponding confidence intervals calculated with four different beginning years (1980,
296 1981, 1982, 1983), four different ending years (2015, 2016, 2017, 2018), and change-
297 point years from 1998 to 2013. The trends and confidence intervals in Figures 2g-j are
298 the same as that in Figures 2c-f, except that the extreme value in 2002 is removed. The
299 positive trend from the early 1980s to the 21st century remains significant regardless of
300 different beginning years and ending change-point years (Figs. 2c-j). However, Figures
301 2c-f and Figures 2g-j indicate that the positive value of the trend is decreasing gradually
302 when the period is prolonged, which is apparently attributed to the negative trend with
303 the beginning change-point year of around 2000. Although the negative trend from the
304 change-point year to ending year becomes less significant when the value in 2002 is

removed, it remains significant in some periods, which are also illustrated on diagrams of latitude-pressure profiles (Fig. S2). Therefore, the weakening of stratospheric wave activities in early austral spring since the early 2000s is robust. In this paper, we take the year 2000 as the beginning year of the weakening trend to simplify descriptions in the following discussion.

Figure 3 shows the trends of tropospheric wave sources in September since 2000. There is a significant positive trend of the wave-1 component in 500 hPa geopotential height over the southern Indian ocean and a significant negative trend over the southern Pacific, which form an out-of-phase superposition on its climatology (Fig. 3b). The trend pattern of wave-2 component is also out-of-phase with its climatology, although it is not significant (Fig. 3c). The above features still maintain when the values in 2002 are removed (Figs. S3b, c), implying that the southern hemispheric tropospheric wave sources in early austral spring have weakened since 2000, which is also reflected in the decrease of tropospheric vertical wave flux (Figs. 3d, e; Figs. S3d, e).

4. Response of Antarctic stratospheric wave activity to ozone recovery

Previous studies have suggested that ozone depletion and recovery are important to climate shift that occurred around 2000 in the southern hemisphere during austral summer (e.g., Son et al., 2008; Thompson et al., 2011; Barnes et al., 2013; Banerjee et al., 2020). The impacts of stratospheric ozone changes on Antarctic wave propagation during austral summer has also been examined in previous studies (e.g., Hu et al., 2015). However, whether ozone recovery in September explains the weakening of stratospheric planetary waves at the same month remains unclear. The correlation

between detrended time series of September Antarctic total column ozone (TCO) derived from SBUV and stratospheric vertical wave flux (Fz) is 0.70 (p=0.0011) during 2000-2017. The increase of wave activity in polar stratosphere causes heating effects and suppresses the formation of PSCs, and hence, slow down the ozone depletion (e.g., Shen et al. 2020a). Therefore, the Antarctic ozone and stratospheric wave activity show statistically significant positive correlation. Theoretically, heating effects caused by ozone recovery in Antarctic stratosphere may also decelerate the Antarctic stratospheric polar vortex and induce more waves to propagate into stratosphere (Andrews et al., 1987; Holton et al., 2004). These preliminary analysis cannot verify that the ozone recovery is responsible for weakening of stratospheric wave activity. The role of ozone recovery in stratospheric wave changes needs to be further explored by model simulations. In this section, we use a group of time-slice experiments (O3ctrl and O3sen) to address this issue.

Figure 4 shows the time series and piecewise trends of September TCO in the Antarctic during 1980-2017. As reported by previous studies (e.g., Angell and Free, 2009; Banerjee et al., 2020; Krzyścin, 2012; Solomon et al., 2016; WMO, 2011; Zhang et al., 2014), the Antarctic ozone show a significant decline during 1980-2000 (Figs. 4a, b, c) and a slight recovery during 2001-2017 (Figs. 4a, d, e). The recovery trend is calculated with data in 2002 removed because the large poleward transport induced by SSW in 2002 leads to extreme values of ozone (e.g. Solomon et al., 2016). In addition, the correlation of TCO between MERRA-2 and SBUV datasets is 0.61 ($p=4.5\times10^{-5}$), suggesting the changes of TCO derived from the reanalysis dataset and the observations

have a good consistency. Thus, in order to get three-dimensional structure of ozone changes, the ozone data from MERRA-2 are used to make forcing fields for CESM. As described in Section 2, a control experiment (O3ctrl) forced by climatological ozone and a sensitive experiment forced by the linear increment of global ozone in September during 2001-2017 are conducted to explore the impacts of ozone recovery. The pattern of ozone forcing fields is similar to its trend patterns (Figs. 4d, e; Figs. 5a, b). Other details of these two experiments have been given in Section 2 and Table 2.

Fig. 6 and Fig. 7 show the responses of wave activity and wave propagation environment forced by O3sen. Note that the significant ozone recovery over south pole mainly appears in lower stratosphere (about 200 hPa to 50 hPa) (Fig. 4e). In most southern polar regions from 50 hPa to 3 hPa, the ozone recovery is not significant (Fig. 4e). The features are attributed to limitation of ODSs emission and reduction of heterogeneous reaction on PSCs, which mainly distribute in lower stratosphere (e.g., Solomon, 1999). Ozone recovery in polar lower stratosphere absorbs more ultraviolet radiation and causes cooling in Antarctic troposphere (Fig. 6b). To maintain thermal balance, zonal wind accelerates below 200 hPa over 60°S-70°S (Fig. 6a).

The changes of zonal wind and temperature forced by ozone recovery induce changes in wave propagation environment. The refractive index (RI) is a good matric to reflect the atmosphere state for wave propagation. Theoretically, planetary waves tend to propagate into large RI regions (Andrews et al., 1987). The responses of RI and its terms are shown in Figs. 6c-f. Note that the second term of RI does not change with atmospheric state and the third term of RI is insignificant compared to the first term

(Hu et al., 2019). Previous studies indicate that changes in zonal mean potential vorticity meridional gradient $\bar{q}_{\varphi}$ could explain the changes in RI in middle and high latitudes (e.g. Hu et al., 2019; Simpson et al., 2009). Consistent with these studies, the pattern of $\bar{q}_{\varphi}$ show some similarity with pattern of RI (Figs. 6c, d), especially in lower stratosphere over subpolar regions (Figs. 6c, d). According to the Eq. (5), the first term of $\bar{q}_{\varphi}$ does not change with atmospheric state. Therefore, the second term ($-[\frac{(\bar{u}\cos\varphi)_{\varphi}}{\cos\varphi}]_{\varphi}$, hereafter uyy term or barotropic term) and the third term ($(-\frac{f^2}{\rho_0}(\rho_0\frac{\bar{u}_z}{N^2})_z$, hereafter uzz term or baroclinic term) are investigated. Note that the pattern of responses in baroclinic term is similar with $\bar{q}_{\varphi}$ (Figs. 6d, f). The uzz term also can be written as $(\frac{f^2}{HN^2}+\frac{f^2}{N^4}\frac{dN^2}{dz})\bar{u}_z-\frac{f^2}{N^2}\bar{u}_{zz}$. Meanwhile, zonal wind acceleration in upper troposphere weakens the vertical shear of u ($\bar{u}_z$) around 200 hPa over subpolar regions, inducing a decrease of baroclinic term and RI in upper troposphere and lower stratosphere (UTLS) over 60°S-70°S (Figs. 6d, f). The response of RI induces a slight decrease of vertical wave flux in UTLS over subpolar regions (Fig. 7a), which is mainly contributed by its wave-1 component (Fig. 7b). However, the changes of wave activity in UTLS are not significant in ensemble mean of simulations (Figs. 7a, b, c). Meanwhile, note that the responses of zonal wind and temperature to ozone recovery are not significant above 50 hPa over subpolar regions (Figs. 6a, b), inducing negligible changes of wave propagation environment (Fig. 6c) and wave activity (Fig. 7) in middle and upper stratosphere.

In a word, the significant ozone recovery in Antarctic lower stratosphere changes

wave propagation in upper troposphere and lower stratosphere to some extent. However, these weak responses still cannot explain the significant decrease of stratospheric wave flux in September.

5. Role of SST trends in the weakening of Antarctic stratospheric wave activities

In this section, we further explore factors responsible for the weakening of tropospheric wave sources and stratospheric wave activities since the early 2000s in early austral spring. Many studies reported that SST variations can affect stratospheric climate (e.g., Li, 2009; Hurwitz et al., 2011; Lin et al., 2012; Hu et al., 2014; Hu et al., 2018; Tian et al., 2017; Xie et al., 2020). Hu & Fu (2009) also attributed the strengthened stratospheric wave activities in the southern hemisphere to SST trend from the early 1980s to the early 2000s. Furthermore, global SST in September during 2000-2017 also has a significant trend. The significant warming pattern is mainly found over the southern Indian ocean, the southern Atlantic ocean, the eastern and western equatorial Pacific, the western equatorial and Northern Atlantic ocean (Fig. 8b). A significant cooling pattern is located over the southeast Pacific (Fig. 8b). In addition, the transitions around 2000 exist in SST time series over some regions. In the southern Indian ocean, SST shows insignificant trend during 1980-2000 and significant warming trend during 2000-2017 (Fig. 8c). The subtropical Pacific ocean in east of Australia is linked with the Pacific-Southern America (PSA) wave train (e.g. Shen et al., 2020b), and the SST there shows significant warming trend during 1980-2000 and insignificant trend during 2000-2017. The SST in southeast Pacific shows insignificant trend during

414 1980-2000 and significant cooling during 2000-2017 (Fig. 8e). Trends of SST in
415 southern Atlantic ocean are opposite during these two piecewise periods, showing
416 significant cooling during 1980-2000 and significant warming during 2000-2017. It is
417 apparent that the spatial pattern of SST trend during 2000-2017 is obviously different
418 from that during 1980-2000 (Fig. 8a, b), which may affect the tropospheric wave
419 sources. Thus, it is necessary to analyze the connection between SST trend and wave
420 activity trend since the early 2000s.

421 Figure 9 shows the significance of the trend of principle component (PC) time
422 series of SST in different regions (Figs. 9a-f), and the significance of correlations (Figs.
423 9g-l) between the PC time series and Fz in September during various periods. The trend
424 of PC1 time series in SH region is significant during serval periods (Fig. 9a), while the
425 correlation between PC1 and Fz is only significant with the particular ending year of
426 2015 (Fig. 9g). This feature suggests that the connection between the SST trend in SH
427 region and the trend of stratospheric wave activity is not robust. The correlation
428 between trend of stratospheric wave activity and that of SST in TROP or NH region is
429 also weak (Fig. 9e, f). As for the combined regions, note that the PC2 time series in
430 SHtrop region has a significant trend (Fig. 9d) and the correlation between the PC2 time
431 series in SHtrop and Fz with the beginning year of around 2000 is also significant (Fig.
432 9j) regardless of different ending years. This feature implies that the extratropical
433 southern hemisphere and tropical SST has a robust connection with stratospheric wave
434 activities in early austral spring since the early 2000s. The correlations between Fz and
435 all PC time series in NHtrop (Fig. 9k) and Globe (Fig. 9l) region are not as robust as

436 that between Fz and PC2 time series in SHtrop region (Fig. 9j), indicating that the
437 connection between SST trend in extratropical northern hemisphere and the trend of
438 stratospheric wave activity is weak.

439 Figure 10 shows the first three EOF modes of September SST in SHtrop region
440 during 2000-2017. The second mode (Fig. 10b) shows a great similarity to the spatial
441 pattern of SST trend (Fig. 8b), and the corresponding PC2 time series also has a
442 significant trend (slope=1.71, $p<0.01$). The correlation between PC2 and Fz is
443 significant (r=-0.56, p=0.016) and the correlation coefficient remains significant (r=-
444 0.46, p=0.065) at the 90% confidence level when the value in 2002 is removed. This
445 result suggests that the SST trend in SHtrop region is closely related to the recent
446 weakening of stratospheric wave activities. The first EOF mode is similar to IPO (Fig.
447 10a) and its corresponding principal component is significantly correlated (r=-0.98,
448 $p<0.01$) with the unfiltered IPO index. However, it shows no significant trend (Fig. 10d)
449 and has no significant correlation (Fig. 10g) with stratospheric wave flux, implying that
450 the linkage between the IPO phase change at around 2000 (e.g. Trenberth et al., 2013)
451 and the weakening of Antarctic stratospheric wave activities is weak. The correlation
452 between PC3 and Fz is also not significant (Fig. 10i). Therefore, it is possible that the
453 combined effect of SST trend (the second EOF mode) in the tropical and extratropical
454 southern hemisphere leads to the weakening of stratospheric wave activities in early
455 austral spring since the early 2000s.

456 **6. Simulated changes in Antarctic stratospheric wave activities forced**
457 **by SST trends**

458 The analysis in Section 5 suggests that the SST changes in SHtrop region may
459 contribute to the weakening of the southern hemispheric stratospheric wave activities.
460 Here, numerical experiments sstNH, sstSH, ssttrop and sstSHtrop forced by linear
461 increments of SST in September during 2000-2017 (Fig. 11; more details can be found
462 in Section 2) are conducted to verify the results presented in Section 5.

463 Figure 12 shows the simulated response of 500 hPa geopotential height to SST
464 changes in different regions. The climatological distributions of the wave-1 component
465 (Figs. 12b, e, h, k) and the wave-2 component (Figs. 12c, f, i, l) from the simulations
466 are consistent with that from reanalysis dataset (Figs. 3b, c), indicating that the model
467 can well capture spatial distributions of the atmospheric waves. Note that the wave-1
468 and wave-2 anomalies simulated with SST changes in SH, TROP and SHtrop are all
469 significant. They superpose on the corresponding climatological patterns in an out-of-
470 phase style (Figs. 12e, f, h, i, k, l), indicating that the changes in SST in SH, TROP and
471 SHtrop lead to a weakening of tropospheric wave sources in the extratropical southern
472 hemisphere. However, the predominate wave-1 component of the 500 hPa geopotential
473 height anomaly in the extratropical southern hemisphere forced by the experiment with
474 NH SST change is relatively weak (Fig. 12b). This feature suggests that the SST
475 changes in extratropical northern hemisphere are incapable of inducing a robust
476 response of tropospheric wave sources in the extratropical southern hemisphere.

477 Figure 13 shows the simulated responses of stratospheric wave activities in the
478 southern hemisphere to SST changes over different regions. It is apparent that the
479 experiments with SST changes in SH, TROP and SHtrop show significantly weakened

stratospheric wave activities (Figs. 13d, g, j), which are mainly attributed to the responses of the wave-1 component (Figs. 13e, h, k). These results are consistent with the responses of tropospheric wave sources (Figs. 12d, e, g, h, j, k). However, there are no significant anomalies of stratospheric wave flux in the subpolar region in Figures 13a and 13b, which is consistent with the response of corresponding tropospheric wave sources (Figs. 12a, b) and the weak correlation between Fz and PC time series of SST in NH region (Fig. 9i). The result here suggests that the response of southern hemisphere stratospheric wave activities to SST trend in NH region is weak.

The results of stratospheric vertical wave flux over 50°S-70°S derived from the 100 ensemble members of each experiment are shown in Figure S4, and the frequency distributions of them are displayed in Figure 14. Compared to the blue fitting curves, the red fitting curves shift to the left as shown in Figs. 14b, 14c and 14d, suggesting that the SST changes in SH, TROP and SHtrop regions weaken the upward propagation of stratospheric wave flux. The area-weighted anomalies of vertical E-P flux in the subpolar region of the southern hemisphere induced by SST changes in SH, TROP and SHtrop regions are -0.084×10^5 kg·s^{-2}, -0.12×10^5 kg·s^{-2} and -0.13×10^5 kg·s^{-2}, respectively. The sum of the anomalies forced by sstSH and ssttrop is not equal to the anomaly forced by sstSHtrop, which may be resulted from non-linear interactions between the responses of wave activities to SST trends in SH region and TROP region. The weakening of stratospheric wave activities forced by SST increment in the tropical region is more significant than that in extratropical southern hemisphere (Figs. 14b, c, e), implying that the SST trend in the tropical region contributes more to the weakening

of stratospheric wave activities since 2000. Meanwhile, it is apparent that the weakening of the southern hemisphere stratospheric wave activities forced by sstSHtrop is the most significant among all the sensitive experiments (Fig. 14e). The reduction of vertical E-P flux over (50°S-70°S, 200 hPa-10 hPa) forced by sstSHtrop is approximately 12%. These modeling results indicate that the weakening of the Antarctic stratospheric wave activities in September since 2000 is induced mainly by the combined effects of SST trends in the tropical and extratropical southern hemisphere. It also explains why the independent correlation between Fz and PC time series obtained over SH or TROP region is not as significant as that between Fz and PC time series obtained over SHtrop region (Figs. 9g, h, j). Moreover, the mean linear increment of area-weighted vertical E-P flux from 200 hPa to 10 hPa over 70°S-50°S in September during 2000-2017 derived from four reanalysis datasets is about -0.38×10^5 kg·s^{-2}. Therefore, the contribution of SST trend over 20°N-70°S (the SHtrop region) to the weakening of stratospheric activities is approximately 34%.

In addition, the reanalysis datasets show that the Brewer-Dobson circulation related to wave activities in the stratosphere weakened significantly in early austral spring during 2000-2017 (Fig. 15b), which is contrary to the intensified trend during 1980-2000 (Fig. 15a). The transition of BDC around 2000 is believed to be associated with ozone depletion and recovery (e.g., Polvani et al., 2017; Polvani et al., 2018). However, our modeling results suggest that the SST trend is responsible for the weakening of BDC in September since 2000 (Figs. 15d, e, f), The response of BDC to ozone recovery is not significant (Fig. 15c) in September, especially for the branch near

524 the Antarctic. These results indicate that apart from the ozone depletion and recovery
525 the SST trend should also be taken into consideration when exploring the mechanism
526 for the climate transition in the southern hemispheric stratosphere around 2000.

527 Previous studies reported that there is usually a time lag for tropic SST to affect
528 extratropical circulation (e.g., Shaman & Tziperman, 2011). Thus, the impact of tropical
529 SST change before September needs to be further examined. Our simulations indicate
530 that the tropical SST trend in September plays a dominate role in weakening of
531 stratospheric wave activity at the same month, and the effect of tropical SST change
532 before September is negligible compared to that in September (The detailed evidences
533 to address this issue are shown in the appendix).

534 ## 7. Conclusions and Discussions

535 This study analyzes the trend of Antarctic stratospheric planetary wave activities
536 in early austral spring since the early 2000s based on various reanalysis datasets and
537 model simulations. Using the change-point method, we find that the Antarctic
538 stratospheric wave activities in September have been weakening significantly since
539 2000, which means the intensified trend of wave activities noted in previous researches
540 (Hu & Fu, 2009; Lin et al., 2009) are reversed after 2000 in early austral spring. Further
541 analysis suggests that the weakening of stratospheric wave activities is related to the
542 weakening of tropospheric wave sources in extratropical southern hemisphere, which
543 is mainly contributed by the wave-1 component.

544 As the Antarctic ozone also shows clear shift around the 2000, we firstly examine
545 the impact of ozone recovery on Antarctic stratospheric planetary wave activity. Our

simulation results indicate that significant ozone recovery in lower stratosphere changes the atmospheric state for wave propagation to some extent, inducing a slight decrease of vertical wave flux over UTLS region in subpolar southern hemisphere. Meanwhile, the changes of wave activity in middle and upper stratosphere over subpolar region induced by ozone recovery are not significant. Therefore, the ozone recovery has minor contribution to the significant weakening of stratospheric planetary wave activity in September.

EOF analysis and correlation analysis indicate that the stratospheric wave activities in early austral spring during 2000-2017 are related to PC2 of SST over 20° N-70°S (i.e., the SHtrop region). The corresponding EOF2 mode also shows a good similarity to the spatial pattern of SST trend, suggesting that the weakening of stratospheric wave activities is connected to the trend of SST in SHtrop region. Meanwhile, the linkage between the SST trend in NH region and the weakening of stratospheric wave activities is weak. The model simulations also support that the SST changes in SHtrop region lead to a weakening of tropospheric wave sources and stratospheric wave activities. The contribution of SST trend in tropical region to the weakening of stratospheric wave activities is larger than that in the extratropical southern hemisphere. However, the response of tropospheric wave sources and stratospheric wave activities to SST trend in NH region is not significant. The contribution of SST trend over SHtrop region to the weakening of stratospheric wave activities is about 34%. Finally, both reanalysis datasets and numerical simulations indicate that the Brewer-Dobson circulation related to stratospheric wave activity has

568 also been weakening in early austral spring since 2000, which is also attributed to the
569 changes of September SST in tropics and extratropical southern hemisphere.

570 Although many researchers claimed that the climate transition around 2000 in
571 southern hemisphere is related to ozone depletion and recovery (e.g., Barnes et al., 2013;
572 Banerjee et al., 2020), there is no contradiction between our results and these previous
573 studies. Firstly, the southern hemisphere tropospheric circulation (i.e., the SAM index,
574 the tropospheric jet position and the Hadley cell edge) shifts related to ozone changes
575 in these previous studies basically occurred in austral summer (e.g., Son et al, 2008;
576 Thompson et al., 2011; Barnes et al, 2013; Banerjee et al., 2020). These tropospheric
577 circulation changes are induced by downward coupling of circulation anomalies in the
578 stratosphere (e.g., Thompson et al., 2011) during October and November, when solar
579 radiation covers the entire Antarctic and causes heating effects. However, the Antarctic
580 stratospheric circulation response to ozone variation in September is not as strong as
581 that in October or November (e.g., Thompson et al., 2011, Figs. 1b, d) because solar
582 radiation can only reach part of Antarctic stratosphere during a majority period of
583 September. This implies that the response of atmospheric state in September to
584 Antarctic stratospheric ozone change is not significant. Secondly, the FWSC
585 component used in this study is an atmospheric module with prescribed SST and forcing
586 gases. Therefore, our model results only indicate that the weakening of stratospheric
587 wave activity can be attributed to SST changes, while the impact of ozone change in
588 middle and low latitudes on SST cannot be determined based on these simulations.
589 Whether the transition signal of Antarctic stratospheric ozone is stored in the ocean

590 needs more efforts to explore. This is an issue beyond the scope of this study and further
591 investigation is necessary by using a fully coupled earth system model.

592 The southern hemisphere stratospheric wave activity trend from the early 1980s to
593 the early 2000s has been investigated by Hu and Fu (2009) (hereafter HF2009) and
594 hence is not discussed in detail in the above. HF2009 attributed the strengthening of
595 stratospheric wave activity in austral spring during 1979-2006 to the SST trends as well,
596 however, they gave no more details about the trends of tropospheric wave sources. In
597 this study, trends of tropospheric wave sources in September during 1980-2000 derived
598 from MERRA-2 data is analyzed, and we also conducted an experiment (sstSHtrop)
599 forced by the changes in September SST during 1980-2000 over 20°N-70°S (see Fig.
600 S9 for applied SST anomalies). The model result indicates that the SST changes over
601 20°N-70°S contribute to intensification of wave-2 component of tropospheric wave
602 sources (Fig. S10f) and weakening of the wave-1 component (Fig. S10e), which is
603 overall analogous to the trends derived from MERRA-2 data (Figs. S10b, c).
604 Accordingly, the simulated wave-2 component of wave flux increases significantly in
605 the stratosphere (Fig. S10h), while the response of the wave-1 component is not
606 significant (Fig. S10i). In a word, the results from sstSHtrop80 suggest that the SST
607 changes over 20°N-70°S induce a strengthening of stratospheric wave activity in
608 September during 1980-2000. But it cannot explain the intensified wave-1 component
609 of the stratospheric wave activity shown in Fig. 1b. A more detailed attribution of the
610 trend of Antarctic stratospheric wave activity during 1980-2000 needs much more
611 efforts.

The simulated stratospheric eddy heat flux (Fig. 11b in HF2009) forced by observed time-varying SST in HF2009 is relatively weak compared to that derived from reanalysis data (Fig. 6b in HF2009). Similarly, Wang and Waugh (2012) (hereafter WW2012) used stratosphere-resolving chemistry-climate model forced by time-varying factors to evaluate the trends of stratospheric temperature, residual circulation as well as wave activity during recent decades, and the trend of cumulative eddy heat flux shown in their paper is not significant (Fig. 6 in WW2012). Additionally, Polvani et al. (2018) used time-varying ODSs that cover the period from 1960s to 2080s to simulate Brewer-Dobson circulation and attained an obvious trend transition around 2000. We had also tried to conduct transient experiments forced by time-varying SST derived from ERSST v5 with different initial conditions, however, the trends of wave activities in the transient simulations are so weak, though the opposite trend signs exist during 1980-2000 and 2000-2018 (Table S2, Fig. S11). The significance of simulated trend may be related to model performance and the length of simulating period. As the period we focus is relatively short and our purpose is attribution rather than generating a real trend, we perform the ensemble time-slice experiments in this study, which are also used in many other previous researches (e.g., Hu et al., 2018; Kang et al., 2011; Zhang et al., 2016) to attribute trends in the atmosphere. In addition, most of the current climate models cannot generate a realistic wave activity trend as waves in the atmosphere are linked with various processes and factors (e.g., Baldwin & Dunkerton, 2005; Garcia & Randel, 2008; Labitzke, 2005; Shindell et al., 1999; Shu et al., 2013; Xie et al., 2008).

Data availability:

The ERA-Interim is available at: https://apps.ecmwf.int/datasets/data/interim-full-daily/levtype=sfc/. The MERRA-2 is available at: https://disc.gsfc.nasa.gov/datasets?keywords=%22MERRA-2%22&page=1&source=Models%2FAnalyses%20MERRA-2. The JRA-55 is available at: https://jra.kishou.go.jp/JRA-55/index_en.html#download. The NCEP-2 is available at: http://www.cpc.ncep.noaa.gov/products/wesley/reanalysis2/. The ERSST v5 dataset is available at: https://www1.ncdc.noaa.gov/pub/data/cmb/ersst/v5/netcdf/. The observations of TCO from SBUV v 8.6 satellite dataset are available at: https://acd-ext.gsfc.nasa.gov/Data_services/merged/data/sbuv_v86_mod.int_lyr.70-18.za.r7.txt. The unfiltered IPO index derived from ERSST v5 dataset is available at: https://psl.noaa.gov/data/timeseries/IPOTPI/tpi.timeseries.ersstv5.data.

Author contributions:

Yihang Hu conducted experiments, produced figures and tables, organized and wrote the manuscript. Wenshou Tian, Jiankai Zhang and Tao Wang contributed to revise the manuscript. Mian Xu helped to design experiments.

Competing interests:

The authors declare that they have no competing interest.

Acknowledgements:

This work is supported by the National Natural Science Foundation of China (41630421 and 42075062). We thank Institute Pierre Simon Laplace (IPSL), NCEP and

NCAR and Japan Meteorological Agency (JMA) for providing ERA-Interim, NCEP-2 and JRA-55 datasets. We thank National Aeronautics and Space Administration (NASA) for providing MERRA-2 dataset and SBUV v8.6 satellite dataset. We thank National Oceanic and Atmospheric Administration (NOAA) for providing ERSST v5 dataset and IPO index. We also thank the scientific team at NCAR for providing CESM-1 model. Finally, we thank the computing support provided by the Supercomputing Center and the College of Atmospheric Sciences from Lanzhou University.

APPENDIX

Analysis of time lag for tropical SST affects Antarctic stratospheric wave activity

As stated in the Section 2, the tropical SST anomalies (the linear inecrements) in experiment ssttrop are also applied in July and August (Fig. S5a, b) to avoid abrupt SST variations from month to month, and the two months are taken as spin-up time. Therefore, whether the SST forcing in July and August also contribute to the weakening of Antarctic stratospheric wave activity in September or not cannot be justified based on the experiment ssttrop only. Here, we performed an additional experiment ssttropAug without September SST anomalies (Fig. S5f) to clarify whether the weakening of Antarctic stratospheric wave activity is induced by the tropical SST trend at the same month. Like other numerical experiments described in Table 1, the ssttropAug also includes 100 ensemble members that run from July to September forced by the same initial conditions from the 21st year to the 120th year in July generated by

678 free run. The detailed descriptions of ssttropAug and other relevant experiments in the
679 manuscript are displayed together in the Table S1 for comparison. Figure S5 shows the
680 applied global SST anomalies in ssttrop and ssttropAug from July to September.

681 The responses of tropospheric wave sources and stratospheric wave activities in
682 ssttropAug are shown in Figs. S6a-c and Figs. S6d-f, respectively. Note that the
683 anomalies of subpolar tropospheric geopotential height in September forced by changes
684 in tropical SST in August does not superpose on their climatological patterns in an
685 evident out-of-phase style (Figs. S6a-c). The anomaly of wave-1 component of
686 geopotential height shows a slight in-phase overlap with its climatology over subpolar
687 region (Fig. S6b). Accordingly, the responses of stratospheric wave activities over
688 subpolar of southern hemisphere are not significant (Figs. S6d-f). The results here
689 suggest that, the decrease of September vertical wave flux induced by SST changes in
690 August is negligible comparing to that in the experiment with anomalous SST forcing
691 in September (Figs. S6g), and the tropical SST trend in September plays a dominate
692 role in weakening of stratospheric wave activity at the same month.

693 Furthermore, we also use a linear barotropic model (LBM) (e.g., Shaman &
694 Tziperman, 2007; Shaman & Tziperman, 2011) to quantify the time scale for
695 propagation of tropical anomalies to high latitudes. The LBM are developed to solve
696 the barotropic vorticity equation, which is given as Eq. (A1):

697 $$J(\bar{\psi}, \nabla^2\psi') + J(\psi', \nabla^2\bar{\psi} + f) + \alpha\nabla^2\psi' + K\nabla^4\nabla^2\psi' = R \quad \text{(A1)}$$

698 where the Jacobian $J(A,B)$ is

699 $$J(A,B) = \frac{1}{r^2}\left(\frac{\partial A}{\partial \lambda}\frac{\partial B}{\partial \mu} - \frac{\partial A}{\partial \mu}\frac{\partial B}{\partial \lambda}\right) \quad \text{(A2)}$$

the forcing function R is

$$R = -(f + \nabla^2 \overline{\psi})D \quad \text{(A3)}$$

ψ is the streamfunction, f is the Coriolis force, α is the Rayleigh coefficient, K is the diffusion coefficient, λ is the longitude, $\mu = \sin(\theta)$, θ is the latitude, r is the earth's radius and D is the divergence.

We use the wave-1 component of streamfunction derived from ensemble mean of sstctrl as the background field. In LBM, the initial anomaly is given by the divergence. The divergence forcing field is limited in 40°E-140°W, 10°S-0° (Fig. S7) to ensure that the tropical initial anomaly of streamfunction superpose on its background field in an out-of-phase style. We set $D = -7.9 \times 10^{-7}\ s^{-1}$, which is the mean divergence over the forcing region. The LBM simulated streamfunction anomalies are shown in Figs. S8b-i. Note that the anomalies in tropics only take a few days to arrive the high latitudes in southern hemisphere. After about four days, a stable anti-phase superposition of streamfunction is well established in extratropical southern hemisphere (Figs. S8f-i). These results are supported by previous studies (e.g., Shaman & Tziperman, 2011), which also indicate that the horizontal propagation of anomaly in atmosphere takes a few days.

Previous studies also reported that it takes about 4 days for wave-1 to propagate from troposphere into stratosphere and 1-2 days for wave-2 (e.g., Randel, 1987). Thus, the tropical oceans affect the stratosphere at mid-high latitudes with a lag of several days. However, the SST forcing field applied in CESM is on monthly scale. It is reasonable to use September SST trend to drive and explain the trends of extratropical

722 circulation and wave activity at the same month.

723

724 **Reference**

725 Andrews, D. G., Holton, J. R., & Leovy, C. B.: Middle atmosphere dynamics, (p. 489), San Diego,
726 Calif: Academic Press Inc, 1987.

727 Angell, J. K., & Free, M.: Ground-based observations of the slowdown in ozone decline and onset
728 of ozone increase, J. Geophys. Res., 114(D7), D07303,
729 https://doi.org/10.1029/2008JD010860, 2009.

730 Baldwin, M., P., Dunkerton, T. J.: Stratospheric harbingers of anomalous weather regimes, Science.
731 https://doi.org/10.1126/science.1063315, 2001.

732 Baldwin, M., P., Dunkerton, T., J.: The solar cycle and stratosphere-troposphere dynamical coupling.
733 J. Atmos. Sol-Terr. Phy., 67(1-2), 71-82, https://doi.org/10.1016/j.jastp.2004.07.018, 2005.

734 Baldwin, M., Hirooka, T., O'Neill, A., Yoden, S., Charlton, A. J., Hio, Y., & Yoden, S.: Major
735 stratospheric warming in the Southern Hemisphere in 2002: Dynamical aspects of the
736 ozone hole split, SPARC Newsletter, 20, 24–26, 2003.

737 Banerjee, A., Fyfe, J. C., Polvani, L. M., Waugh D., Chang K. L.: A pause in Southern Hemisphere
738 circulation trends due to the Montreal Protocol, Nature, 579(7800), 544–548,
739 https://doi.org/10.1038/s41586-020-2120-4, 2020.

740 Birner, T., & Bönisch, H.: Residual circulation trajectories and transit times into the extratropical
741 lowermost stratosphere, Atmos. Chem. Phys., 11(2), 817–827, https://doi.org/10.5194/acp-
742 11-817-2011, 2011.

743 Bosilovich, M., Akella, S., Coy, L., Cullather, R., Draper, C., Gelaro, R. and Suarez, M.: MERRA-2:

744 Initial Evaluation of the Climate, NASA Technical Report Series on Global Modeling and Data
745 Assimilation, 43, 139, 2015.
746 Charney, J. G., & Drazin, P. G.: Propagation of planetary-scale disturbances from the lower into the
747 upper atmosphere, J. Geophys. Res., 66(1), 83-109,
748 https://doi.org/10.1029/JZ066i001p00083, 1961.
749 Dee, D. P., Uppala, S. M., Simmons, A. J., Berrisford, P., Poli, P., Kobayashi, S., et al.: The ERA-
750 Interim reanalysis: Configuration and performance of the data assimilation system, Q. J.
751 Roy. Meteor. Soc., 137(656), 553–597, https://doi.org/10.1002/qj.828, 2011.
752 Gabriel, A., H. Körnich, Lossow, S., Peters, D. H. W., & Murtagh, D.: Zonal asymmetries in middle
753 atmospheric ozone and water vapour derived from odin satellite data 2001–2010, Atmos.
754 Chem. and Phys., 11(18), 9865-9885, https://doi.org/10.5194/acp-11-9865-2011, 2011.
755 Garcia, R. R., & Randel, W. J.: Acceleration of the brewer-dobson circulation due to increases in
756 greenhouse gases, J. Atmos. Sci., 65(8), 2731-2739.
757 https://doi.org/10.1175/2008JAS2712.1, 2008.
758 Haigh, J. D., Blackburn, M., & Day, R.: The response of tropospheric circulation to perturbations in
759 lower-stratospheric temperature, J. Climate, 18(17), 3672-3685.
760 https://doi.org/10.1175/JCLI3472.1, 2005.
761 Haynes, P. H., M. E. McIntyre, T. G. Shepherd, C. J. Marks, and K. P. Shine.: On the “Downward
762 Control” of Extratropical Diabatic Circulations by Eddy-Induced Mean Zonal Forces, J.
763 Atmos. Sci., 48(4), 651–678, https://doi.org/10.1175/1520-
764 0469(1991)048<0651:OTCOED>2.0.CO;2, 1991.
765 Holton, J.: An introduction to dynamic meteorology, (p. 535), Elsevier Academic Pr., 2004.

Huang, B., Peter W. Thorne, et. al.: Extended Reconstructed Sea Surface Temperature version 5 (ERSSTv5), Upgrades, validations, and intercomparisons, J. Climate, 30(20), 8179-8205, https://doi.org/10.1175/JCLI-D-16-0836.1, 2017.

Hu, D., Tian, W., Xie, F., Shu, J., Dhomse, S.: Effects of meridional sea surface temperature changes on stratospheric temperature and circulation, Adv. Atmos. Sci., 31, 888–900. https://doi.org/10.1007/s00376-013-3152-6, 2014.

Hu, D., Tian, W., Xie, F., Wang, C., Zhang, J.: Impacts of stratospheric ozone depletion and recovery on wave propagation in the boreal winter stratosphere, J. Geophys. Res-Atmos., 120(16), 8299-8317, https://doi.org/10.1002/2014JD022855, 2015.

Hu, D., Guan, Z., Tian, W., & Ren, R.: Recent strengthening of the stratospheric Arctic vortex response to warming in the central North Pacific, Nat. Commun., 9(1), 1697. https://doi.org/10.1038/s41467-018-04138-3, 2018.

Hu, D., Guo, Y., & Guan, Z.: Recent weakening in the stratospheric planetary wave intensity in early winter, Geophys. Res. Lett., 46(7), 3953-3962, https://doi.org/10.1029/2019GL082113, 2019.

Hurwitz, M. M., Newman, P. A., Oman, L. D., & Molod, A. M.: Response of the antarctic stratosphere to two types of El niño events, J. Atmos. Sci., 68(4), 812-822. https://doi.org/10.1175/2011JAS3606.1, 2011.

Hu, Y., & Fu, Q.: Stratospheric warming in southern hemisphere high latitudes since 1979, Atmos. Chem. Phys., 9(13), 4329-4340, https://doi.org/10.5194/acp-9-4329-2009, 2009.

Ialongo, I., Sofieva, V., Kalakoski, N., Tamminen, J., & E. Kyrölä.: Ozone zonal asymmetry and planetary wave characterization during antarctic spring, Atmos. Chem. Phys., 12(5), 2603-

2614, https://doi.org/10.5194/acp-12-2603-2012, 2012.

Kanamitsu, M., Ebisuzaki, W., Woollen, J., Yang, S. K., Hnilo, J. J., Fiorino, M., & Potter, G. L.: NCEP–DOE AMIP-II Reanalysis (R-2), B. Am. Meteorol. Soc., 83(11), 1631–1644. https://doi.org/10.1175/BAMS-83-11-1631, 2002.

Kang, S. M. , Polvani, L. M. , Fyfe, J. C. , & Sigmond, M.: Impact of polar ozone depletion on subtropical precipitation, Science, 332(6032), 951-954, https://doi.org/10.1126/science.1202131, 2011.

Kim, B. M., Son, S. W., Min, S. K., Jeong, J. H., Kim, S. J., Zhang, X., Shim, T., Yoon, J. H.: Weakening of the stratospheric polar vortex by Arctic sea-ice loss, Nat. Commun., 5(1), 4646, https://doi.org/10.1038/ncomms5646, 2014.

Kobayashi, S., Y. Ota, Y. Harada, A. Ebita, M. Moriya, H. Onoda, K. Onogi, H. Kamahori, C. Kobayashi, H. Endo, K. Miyaoka, and K. Takahashi,: The JRA-55 Reanalysis: General specifications and basic characteristics, J. Meteorol. Soc. of Jpn., 93(1), 5-48, https://doi.org/10.2151/jmsj.2015-001, 2015.

Kravchenko, V. O., Evtushevsky, O. M., Grytsai, A. V., Klekociuk, A. R., Milinevsky, G. P., and Grytsai, Z. I.: Quasi-stationary planetary waves in late winter Antarctic stratosphere temperature as a possible indicator of spring total ozone, Atmos. Chem. Phys., 11(10), 28945–28967, https://doi.org/10.5194/acp-12-2865-2012, 2011.

Krzyścin, J. W.: Onset of the total ozone increase based on statistical analyses of global ground-based data for the period 1964 – 2008, Int. J. Climatol., 32(2), 240-246, https://doi.org/10.1002/joc.2264, 2012.

Labitzke, K.: On the solar cycle-QBO relationship: A summary. J. Atmos. Sol-Terr. Phy., 67(1-2),

45-54, https://doi.org/10.1016/j.jastp.2004.07.016, 2005.

Lin, P., Fu, Q., Solomon, S., & Wallace, J. M.: Temperature trend patterns in southern hemisphere high latitudes: novel indicators of stratospheric change, J. Climate, 22(23), 6325-6341. https://doi.org/10.1175/2009JCLI2971.1, 2009.

Lin, P., Fu, Q., & Hartmann, D.: Impact of tropical SST on stratospheric planetary waves in the southern hemisphere, J. Climate, 25(14), 5030-5046. https://doi.org/10.1175/JCLI-D-11-00378.1, 2012.

Li, S.: The influence of tropical indian ocean warming on the southern hemispheric stratospheric polar vortex, Sci. China. Ser. D., 52(3), 323–332, https://doi.org/10.1007/s11430-009-0029-8, 2009.

Li, Y., & Tian, W.: Different impact of central pacific and eastern pacific El ñino on the duration of sudden stratospheric warming, Adv. Atmos. Sci., 34(06), 771-782. https://doi.org/10.1007/s00376-017-6286-0, 2017.

Li, Y., Tian, W., Xie, F., Wen, Z., Zhang, J., Hu, D., & Han, Y.: The connection between the second leading mode of the winter North Pacific sea surface temperature anomalies and stratospheric sudden warming events, Clim. Dynam., 51(1-2), 581-595. https://doi.org/10.1007/s00382-017-3942-0, 2018.

Marsh, D. R., Mills, M. J., Kinnison, D. E., Lamarque, J. F., Calvo, N., & Polvani, L. M.: Climate change from 1850 to 2005 simulated in CESM1 (WACCM), J. Climate, 26(19), 7372-7391. https://doi.org/10.1175/JCLI-D-12-00558.1, 2013.

Neale, R. B., Richter, J., Park, S., Lauritzen, Lauritzen, P. H., Vavrus, S. J., Rasch, P. J., & Zhang, M.:The mean climate of the community atmosphere model (cam4) in forced sst and fully

coupled experiments, J. Climate, 26(14), 5150-5168, https://doi.org/10.1175/JCLI-D-12-00236.1, 2013.

Newman, P. A., & Nash, E. R.: The unusual Southern Hemisphere stratosphere winter of 2002, J. Atmos. Sci., 62(3), 614–628. https://doi.org/10.1175/JAS-3323.1, 2005.

Nishii, K. and Nakamura, H.: Tropospheric influence on the diminished Antarctic ozone hole in September 2002, Geophys. Res. Lett., 31(16), L16103, https://doi.org/10.1029/2004GL019532, 2004.

Polvani, L. M., Wang, L., Aquila, V., & Waugh, D. W.: The impact of ozone depleting substances on tropical upwelling, as revealed by the absence of lower stratospheric cooling since the late 1990s, J. Climate, 30(7), 2523-2534. https://doi.org/10.1175/JCLI-D-16-0532.1, 2017.

Polvani, L. M., Abalos, M., Garcia, R., Kinnison, D., & Randel, W. J.: Significant weakening of Brewer-Dobson circulation trends over the 21st century as a consequence of the Montreal Protocol, Geophys. Res. Lett., 45(1), 401–409, https://doi.org/10.1002/2017GL075345, 2018.

Randel, W. J.: A study of planetary waves in the southern winter troposphere and stratosphere. Part I: Wave structure and vertical propagation, J. Atmos. Sci., 44(6), 917-935, 1987.

Randel, W. J., & Wu, F.: Cooling of the arctic and antarctic polar stratospheres due to ozone depletion, J. Climate, 12(5), 1467-1479. https://doi.org/10.1175/1520-0442(1999)012<1467:COTAAA>2.0.CO;2, 1999.

Shaman, J., & Tziperman, E.: An atmospheric teleconnection linking ENSO and southwestern European precipitation, J. Climate., 24(1), 124-139, https://doi.org/10.1175/2010JCLI3590.1, 2011.

Shaman, J., & Tziperman, E.: Summertime ENSO-North African-Asian Jet teleconnection and implications for the Indian monsoons, Geophys. Res. Lett., 34(11), L11702, https://doi.org/10.1029/2006GL029143, 2007.

Shen, X., Wang, L., & Osprey, S.: The southern hemisphere sudden stratospheric warming of september 2019, Sci. Bull., 65(21), 1800-1802. https://doi.org/10.1016/j.scib.2020.06.028, 2020a.

Shen, X., Wang, L., & Osprey, S.: Tropospheric forcing of the 2019 antarctic sudden stratospheric warming, Geophys. Res. Lett., 47(20), e2020GLO89343, https://doi.org/10.1029/2020GL089343, 2020b.

Shindell, D., T., Miller, R., L., Schmidt, G., A., & Pandolfo, L.: Simulation of recent northern winter climate trends by greenhouse-gas forcing, Nature, 399(6735), 452-455, https://doi.org/10.1038/20905, 1999.

Shirley, D., Stanley, W., & Daniel, C.: Statistics for Research (Third Edition), (p. 627), Hoboken, New Jersey: John Wiley & Sons Inc., 2004.

Shu, J., Tian, W., Hu, D., Zhang, J., Shang, L., Tian, Hu., & Xie, F.: Effects of the quasi-biennial oscillation and stratospheric semi-annual oscillation on tracer transport in the upper stratosphere. J. Atmos. Sci., 70(5), 1370-1389, https://doi.org/10.1175/JAS-D-12-053.1, 2013.

Simpson, I. R., Blackburn, M., & Haigh, J. D.: The role of eddies in driving the tropospheric response to stratospheric heating perturbations, J. Atmos. Sci., 66(5), 1347-1365, https://doi.org/10.1175/2008JAS2758.1, 2009.

Solomon, S., Ivy, D. J., Kinnison, D., Mills, M. J., Neely, R. R., & Schmidt, A.: Emergence of

healing in the antarctic ozone layer, *Science*, 353(6296), 269-274, https://doi.org/10.1126/science.aae0061, 2016.

Solomon, S.: Stratospheric ozone depletion: a review of concepts and history, Rev. Geophys., 37(3), 275-316, https://doi.org/10.1029/1999RG900008, 1999.

Son, S. W., Han, B. R., Garfinkel, C. I., Seo-Yeon, K., Rokjin, P., & Luke, A. N., et al.: Tropospheric jet response to antarctic ozone depletion: an update with chemistry-climate model initiative (CCMI) models, Environ. Res. Lett., 13(5), 054024-. https://doi.org/10.1088/1748-9326/aabf21, 2018.

Son, S. W., P. G. Edwin, K. H. Seo,: The impact of stratospheric ozone recovery on the Southern Hemisphere westerly jet, Science, 320(5882), 1486-1489, https://doi.org/10.1126/science.1155939, 2008.

Susan, E., S., Douglass, A. R., Damon, M. R.: Why do antarctic ozone recovery trends vary?, J. Geophys. Res.-Atmos., 124(15), 8837-8850. https://doi.org/10.1029/2019JD030996, 2019.

Swart, N. C. & Fyfe, J. C.: Observed and simulated changes in the Southern Hemisphere surface westerly wind-stress, Geophys. Res. Lett., 39(16), L16711, https://doi.org/10.1029/2012GL052810, 2012.

Thompson, D., Solomon, S., Kushner, P. England, M., Grise, K. M., Karoly, D. J.: Signatures of the Antarctic ozone hole in Southern Hemisphere surface climate change, Nat. Geosci., 4, 741–749. https://doi.org/10.1038/ngeo1296, 2011.

Tian, W., Li, Y., Xie, F., Zhang, J., Chipperfield, M., & Feng, W., Hu, Y., Zhao, S., Zhou, X., Zhang, Y. & Ma, X.: The relationship between lower-stratospheric ozone at southern high latitudes and sea surface temperature in the east Asian marginal seas in austral spring, Atmos. Chem.

Phys., 17(11), 6705-6722. https://doi.org/10.5194/acp-17-6705-2017, 2017.

Trenberth, K. E., & Fasullo, J. T.: An apparent hiatus in global warming?, Earth's Future, 1(1), 19–32, https://doi.org/10.1002/2013EF000165, 2013.

Wang, T., Tian, W., Zhang, J., Xie, F., Zhang, R., Huang, J. & Hu, D.: Connections between Spring Arctic Ozone and the Summer Circulation and Sea Surface Temperatures over the Western North Pacific, J. Climate, 33(7): 2907–2923, https://doi.org/10.1175/JCLI-D-19-0292.1, 2020.

WMO.: Scientific assessment of ozone depletion: 2010, World Meteorological Organization/United Nations Environment Programme Rep. 52, 516 pp, 2011.

WMO.: Antarctic ozone hole is smallest on record, World Meteorological Organization. Accessed October 2019 at https://public.wmo.int/en/media/news/antarctic-ozone-hole-smallest-record, 2019.

Xia, Y., Xu, W., Hu, Y., & Xie, F.: Southern-hemisphere high-latitude stratospheric warming revisit, Clim. Dynam., 54(3): 1671-1682. https://doi.org/10.1007/s00382-019-05083-7, 2020.

Xie, F., Tian, W., & Chipperfield, M., P.: Radiative effect of ozone change on stratosphere-troposphere exchange. J. Geophys. Res., 113, D00B09, https://doi.org/10.1029/2008JD009829, 2008

Xie, F., Zhang, J., Huang, Z., Lu, J., & Sun, C.: An estimate of the relative contributions of sea surface temperature variations in various regions to stratospheric change, J. Climate, 33(12), 4994-5011, https://doi.org/10.1175/JCLI-D-19-0743.1, 2020.

Yamazaki, Y., Matthias, V., Miyoshi, Y., Stolle, C., Siddiqui, T., Kervalishvili, G., et al.: September

2019 Antarctic sudden stratospheric warming: Quasi-6-day wave burst and ionospheric effects, Geophys. Res. Lett., 47(1), e2019GL086577. https://doi.org/10.1029/2019GL086577, 2020.

Zhang, J., Tian, W., Xie, F., Tian, H., Luo, J., Zhang, J., Liu, W., Dhomse, S.: Climate warming and decreasing total column ozone over the tibetan plateau during winter and spring, Tellus B., 66(1), https://doi.org/10.3402/tellusb.v66.23415, 2014.

Zhang, J., Tian, W. , Chipperfield, M. P. , Xie, F. , & Huang, J.: Persistent shift of the arctic polar vortex towards the eurasian continent in recent decades, Nat. Clim. Change. 6, 1094–1099. https://doi.org/10.1038/nclimate3136, 2016.

Zhang, J., Tian, W., Xie, F., Sang, W., Guo, D., Chipperfield, M., Feng, W., Hu, D.: Zonally asymmetric trends of winter total column ozone in the northern middle latitudes, Clim. Dynam., 52(7-8), 4483-4500, https://doi.org/10.1007/s00382-018-4393-y, 2019a.

Zhang, P., Wu, Y. & Smith, K. L.: Prolonged effect of the stratospheric pathway in linking Barents–Kara Sea sea ice variability to the midlatitude circulation in a simplified model, Clim. Dynam. 50(17), 527–539. https://doi.org/10.1007/s00382-017-3624-y, 2018.

Zhang, R., Tian, W., Zhang, J., Huang, J., & Xu, M.: The corresponding tropospheric environments during downward-extending and nondownward-extending events of stratospheric northern annular mode anomalies, J. Climate, 32(6), 1857-1873, https://doi.org/10.1175/JCLI-D-18-0574.1, 2019b.

Table 1. Configurations of experiments for SST trends.

Experiments	Descriptions

sstctrl	Control run. Seasonal cycle of monthly mean global SST data over 1980-2000 is derived from the ERSST v5 dataset. Fixed values of ozone greenhouse gases and aerosol fields in 2000 are used.
sstNH	As in sstctrl, but with linear increments of SST in September over 2000-2017 in NH (20°N-70°N). The applied global SST anomalies are shown in Fig. 7a.
sstSH	As in sstctrl, but with linear increments of SST in September over 2000-2017 in SH (20°S-70°S). The applied global SST anomalies are shown in Fig. 7b.
ssttrop	As in sstctrl, but with linear increments of SST in September over 2000-2017 in the tropics (20°S-20°N). The applied global SST anomalies are shown in Fig. 7c.
sstSHtrop	As in sstctrl, but with linear increments of SST in September over 2000-2017 in SHtrop (20°N-70°S). The applied global SST anomalies are shown in Fig. 7d.

941 **Table 2.** Configurations of experiments for the ozone recovery trend.

Experiments	Descriptions
O3ctrl	Control run. The seasonal cycle of monthly averaged global SST data over 1980-2000 is derived from ERSST v5 dataset. The seasonal cycle of monthly mean three-dimensional global ozone over 1980-2000 is derived from MERRA-2 dataset. The GHGs and aerosol fields are specified to be fixed values in 2000.
O3sen	As in O3ctrl, but superposed with linear increments of global ozone in September over 2001-2017. The ozone data in 2002 are removed when the linear increments are calculated. The applied ozone anomalies in Southern Hemisphere are shown in Fig. 5.

942 **Table 3.** Correlations of stratospheric vertical wave flux time series (area-weighted

943 from 100 hPa to 30 hPa over 70°S-50°S) between different reanalysis dataset.

	ERA-Interim	JRA-55	MERRA-2	NCEP-2
ERA-Interim	1.00 (p=0.00)	0.99 (p<0.01)	0.98 (p<0.01)	0.93 (p<0.01)
JRA-55		1.00 (p=0.00)	0.98 (p<0.01)	0.93 (p<0.01)
MERRA-2			1.00 (p=0.00)	0.94 (p<0.01)
NCEP-2				1.00 (p=0.00)

944

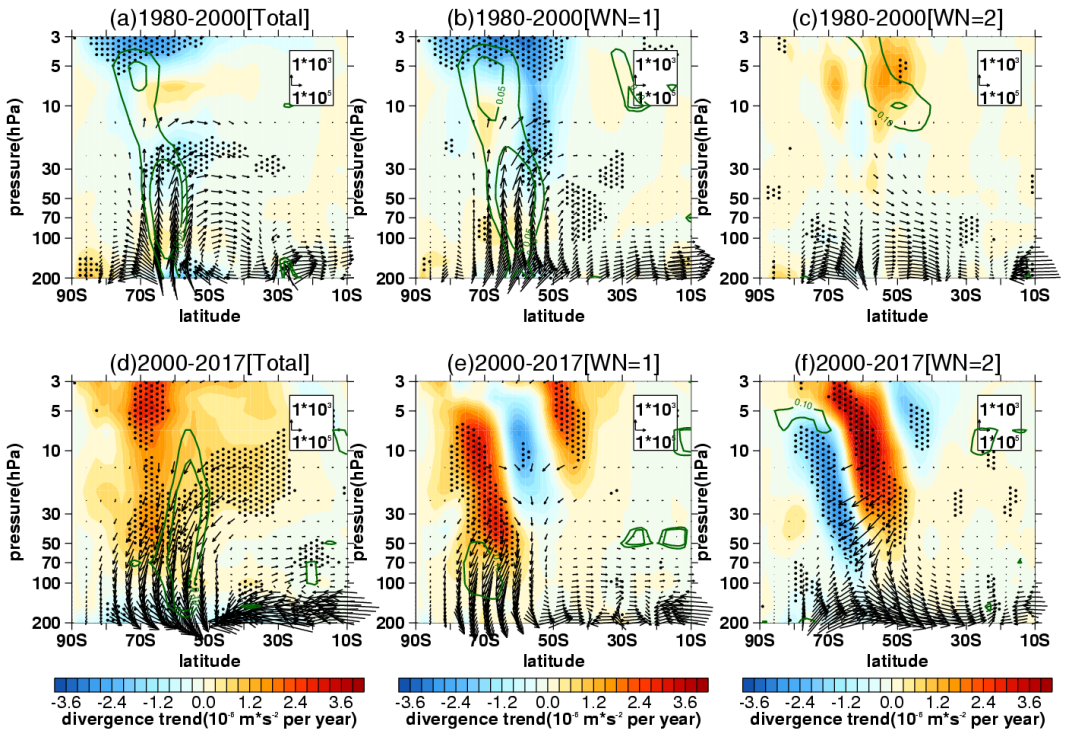

945

946 **FIG. 1.** Trends of southern hemisphere (a, d) stratospheric E-P flux (arrows, units of
947 horizontal and vertical components are 10^5 and 10^3 kg·s^{-2} per year, respectively) and its
948 divergence (shadings) with their (b, e) wave-1 components and (c, f) wave-2
949 components over (a, b, c) 1980-2000 and (d, e, f) 2000-2017 in September derived from
950 MERRA-2 dataset. The stippled regions indicate the trend of E-P flux divergence
951 significant at/above the 90% confidence level. The green contours from outside to
952 inside (corresponding to p=0.1, 0.05) indicate the trend of vertical E-P flux significant

953 at the 90% and 95% confidence level, respectively.

954

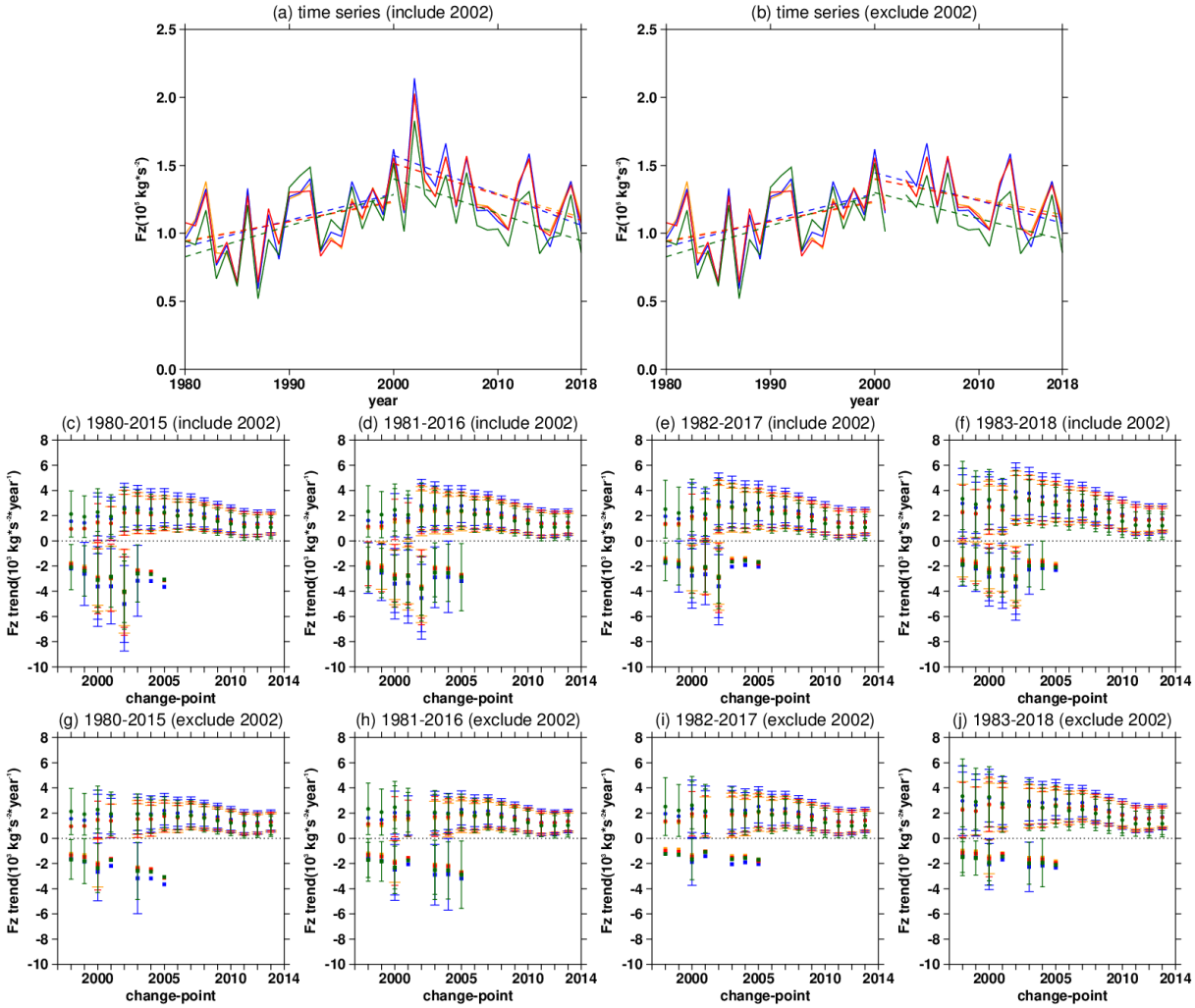

955

956 **FIG. 2.** (a) The mean time series (solid lines) and piecewise (during 1980-2000 and
957 2000-2018) linear regressions (dashed lines) of vertical E-P flux area-weighted from
958 100 hPa to 30 hPa over 70°S-50°S in September during 1980-2018 derived from ERA-
959 Interim (yellow), MERRA-2 (blue), JRA-55 (red) and NCEP-2 (green). Figure (b) is
960 the same as Figure (a), except for that the data in 2002 are removed. (c, d, e, f) The
961 trends (dots) and uncertainties (error bars) calculated during various periods using the
962 change-point method with different beginning and ending years (titles). Circles and

963 squares in Figures (c, d, e, f) represent positive trends from beginning years to change-
964 point years (x-axes) and negative trends from change-point years to ending years,
965 respectively. Different colors of dots and error bars in Figures (c, d, e, f) correspond to
966 colors in Figure (a), which represent trends and uncertainties derived from different
967 datasets. The long and short error bars in same color reflect the 95% and 90%
968 confidence intervals calculated by two-tailed t test. The error bar is omitted when the
969 significance of trend is lower than corresponding confidence level. Negative trends and
970 corresponding uncertainties with the beginning change-point years after 2005 are also
971 omitted, since the trend value shows large fluctuation with shortening of time series.
972 Figures (g, h, i, j) are the same as Figures (c, d, e, f), except that the data in 2002 are
973 removed when calculating trends and uncertainties.

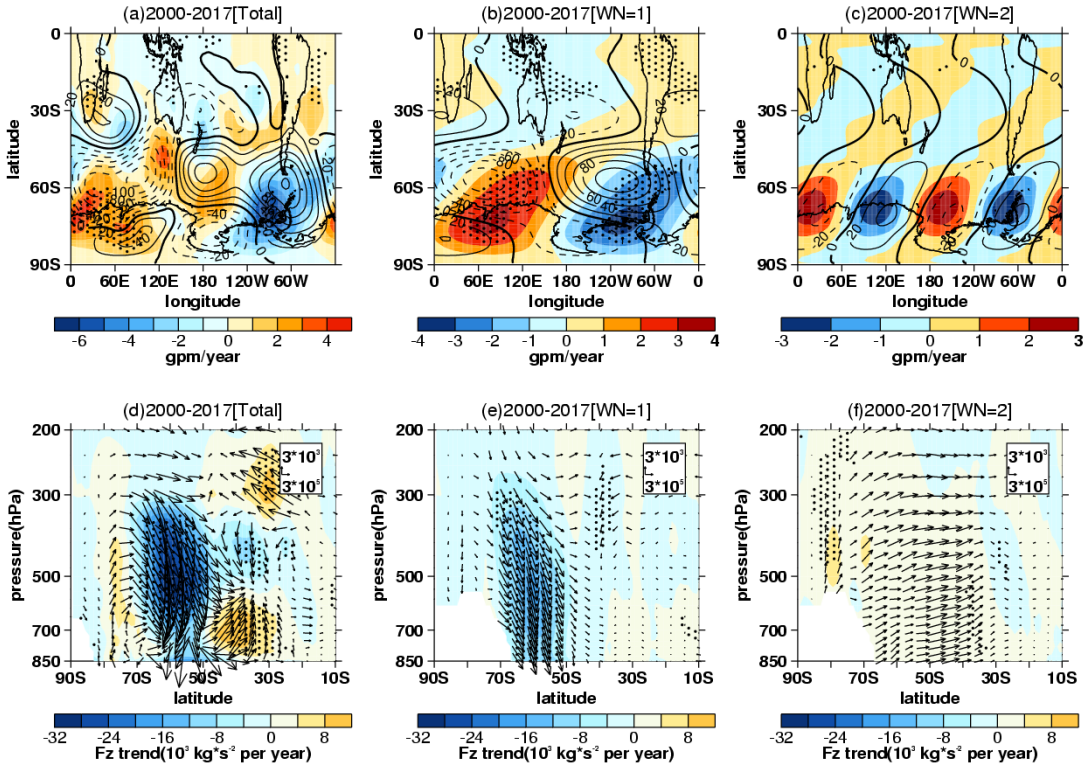

974

975 **FIG. 3.** Trends (shadings) and climatological distributions (contours with an interval
976 of 20 gpm, positive and negative values are depicted by solid and dashed lines

977 respectively, zeroes are depicted by thick solid lines) of southern hemispheric (a) 500
978 hPa geopotential height zonal deviations with their (b) wave-1 component and (c)
979 wave-2 component in September during 2000−2017 derived from MERRA-2 dataset.
980 Trends of southern hemispheric (d) tropospheric E-P flux (arrows, units of horizontal
981 and vertical components are 3×10^5 and 3×10^3 kg s^{-2} per year, respectively) and its
982 vertical component (shading) with their (e) wave-1 component and (f) wave-2
983 component in September during 2000−2017 derived from MERRA-2 dataset. The
984 stippled regions represent the trend significant at/above the 90% confidence level.

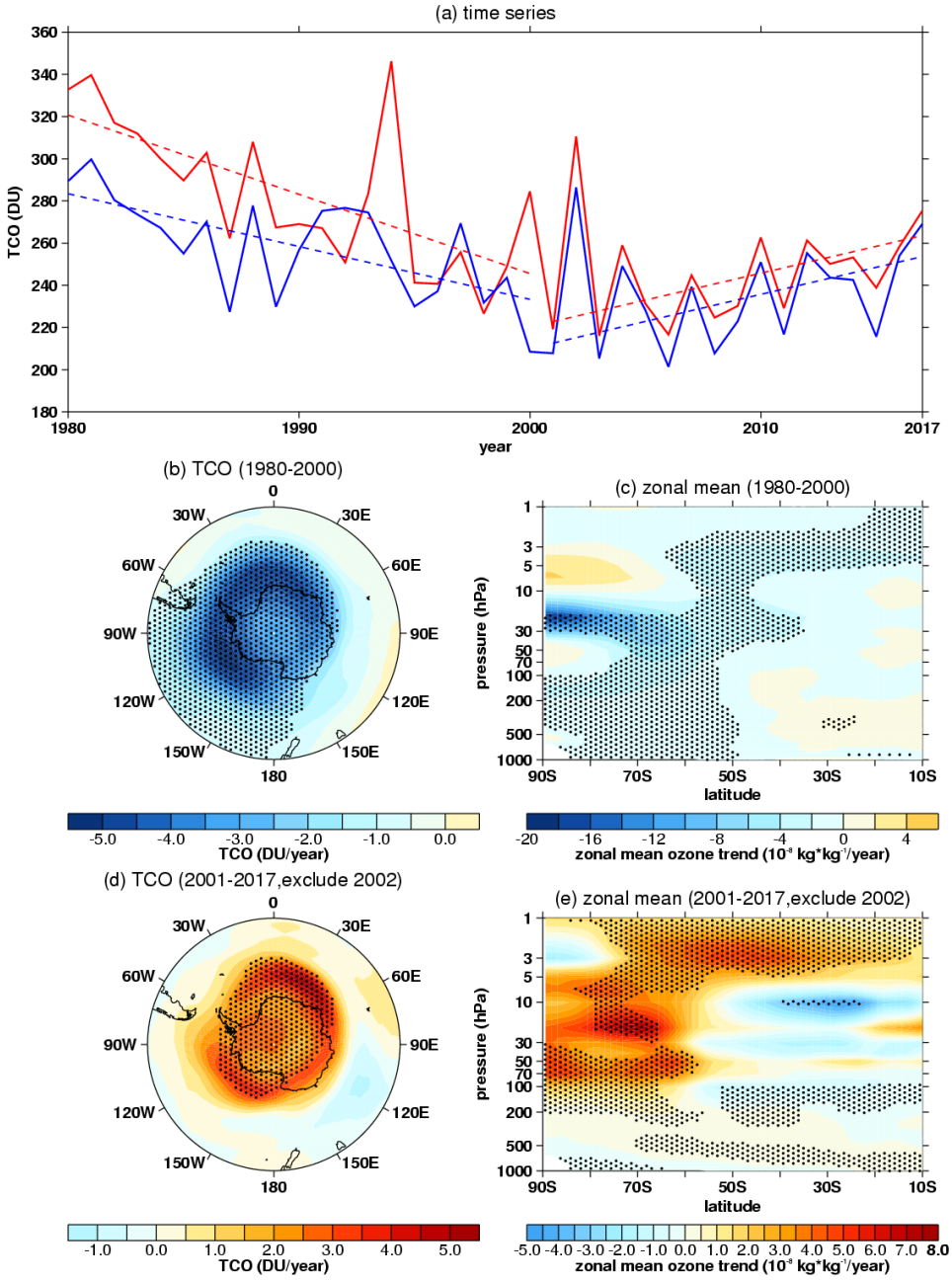

985

986 **FIG. 4**. (a) Time series (solid lines) of aera-weighted total column ozone (TCO) over
987 60°S to 90°S derived from MERRA-2 (red) and SBUV (blue) datasets. The dashed lines
988 represent linear regression of TCO. (b, d) The TCO trends in September during 1980-
989 2000 (b) and 2001-2017 (d) derived from MERRA-2 dataset. The outermost latitudes
990 in Figs. 4c, d are both 40°S. (c, e) The zonal mean ozone trends on latitude-pressure
991 profile in September during 1980-2000 (c) and 2001-2017 (e) derived from MERRA-2

dataset. The stippled regions in Figs. 4b-e represent trends significant at/above the 90% confidence level. Data in 2002 are removed when trends, regressions and significances are calculated in Fig. 4.

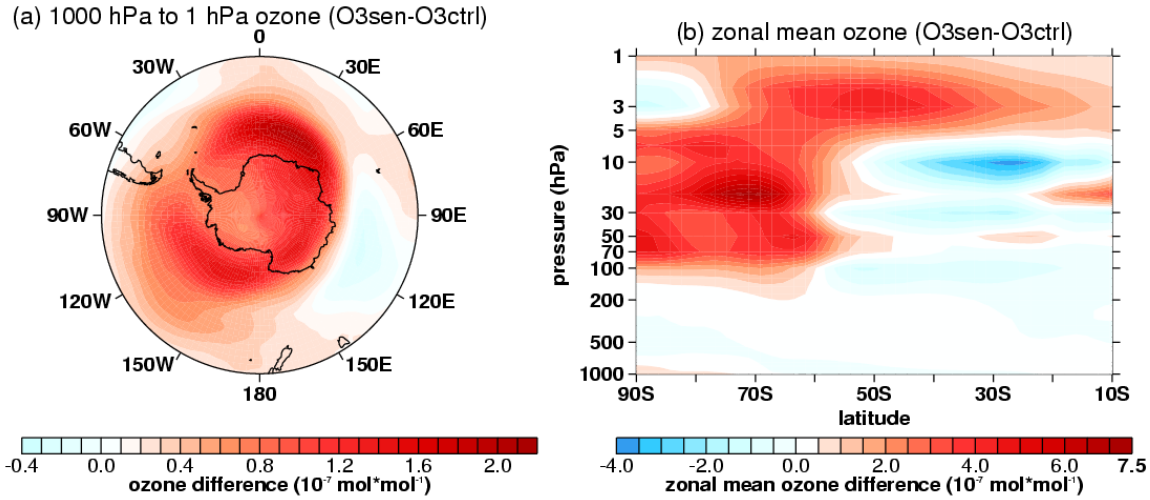

FIG. 5. (a) Difference of horizontal ozone forcing field averaged from 1000 hPa to 1 hPa between O3sen and O3ctrl. The outermost latitude in Fig. 5a is 40 ℃S. (b) Zonal mean difference of ozone forcing fields on latitude-pressure profile in the southern hemisphere between O3sen and O3ctrl.

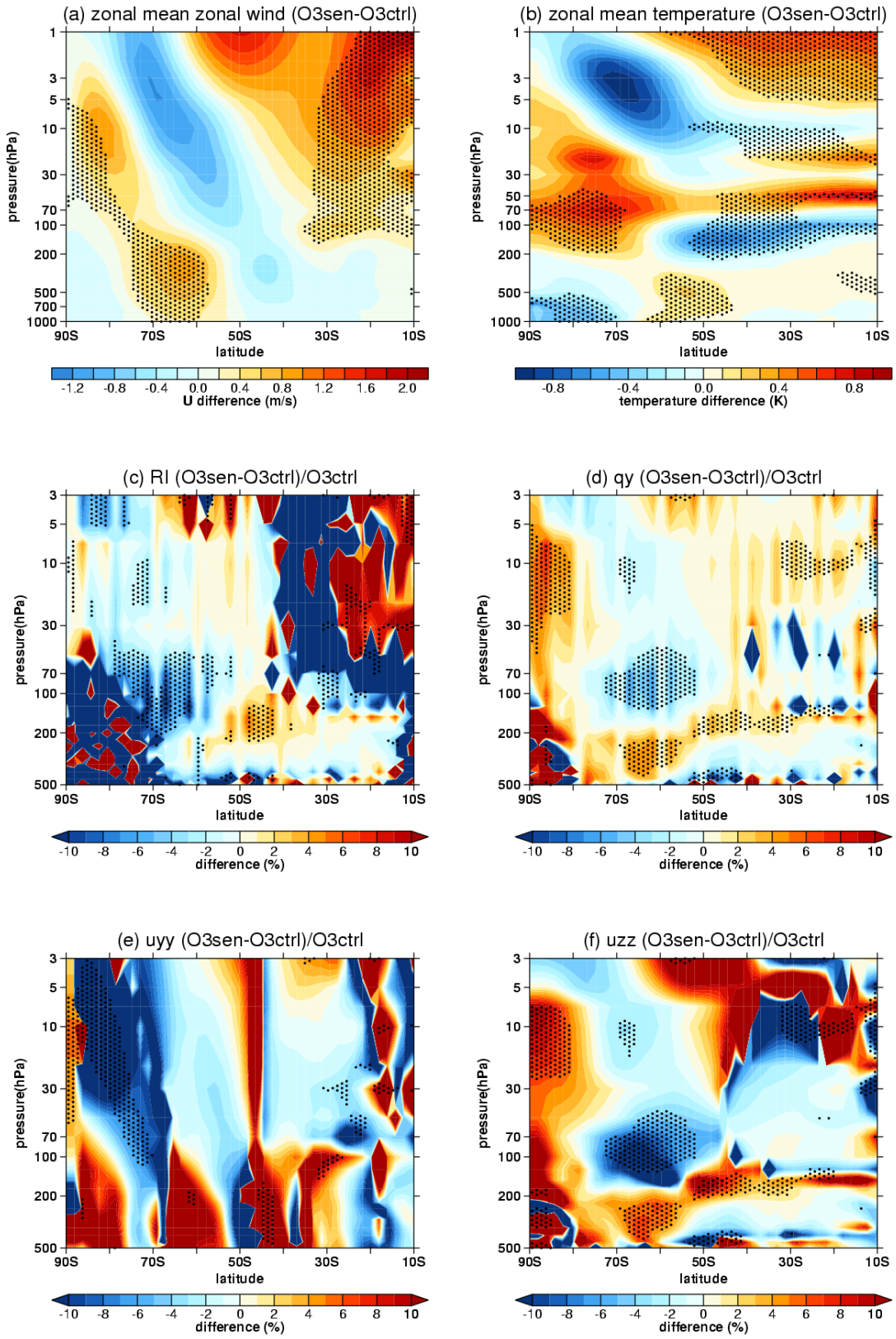

1000

1001 **FIG. 6**. Difference of (a) zonally averaged zonal wind, (b) zonally averaged

temperature, (c) refractive index, (d) $a^2\bar{q}_\varphi$, (e) $-[\frac{(\bar{u}\cos\varphi)_\varphi}{\cos\varphi}]_\varphi$ (uyy term), (f) $-\frac{a^2 f^2}{\rho_0}(\rho_0 \frac{\bar{u}_z}{N^2})_z$ (uzz term) between O3sen and O3ctrl. The stippled regions represent the difference significant at/above 90% confidence level.

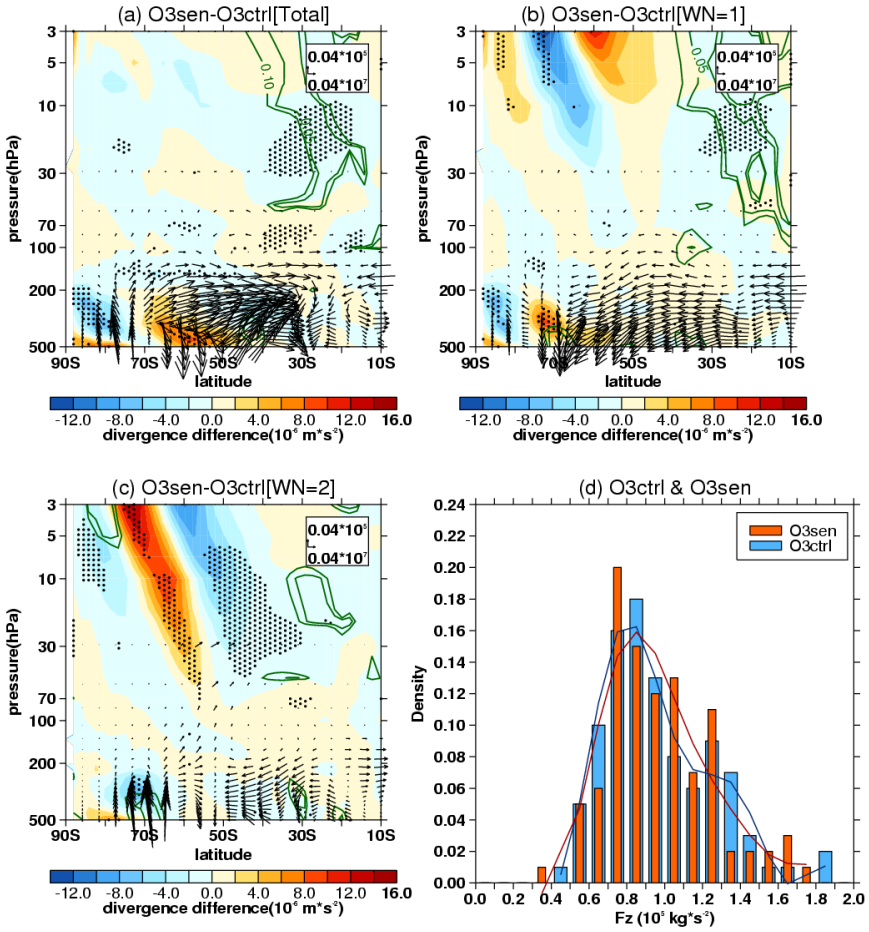

FIG. 7. Differences of (a) stratospheric E-P flux (arrows, units in horizontal and vertical components are 0.04×10^7 and 0.04×10^5 kg s^{-2}, respectively) and its divergence (shadings) with their (b) wave-1 component and (c) wave-2 component between the sensitive experiment (O3sen) and the control experiment (O3ctrl). The stippled regions represent the mean differences of E-P flux divergence significant at/above the 90% confidence level. The green contours from outside to inside (corresponding to p=0.1, 0.05) represent the mean differences of vertical E-P flux significant at the 90% and 95%

confidence levels, respectively. (d) Frequency distributions (pillars, blue for O3ctrl and orange for O3sen) of vertical E-P flux (Fz, area-weighted from 200 hPa to 10 hPa over 70 ℃S-50 ℃S) and it 5-point low-pass filtered fitting curves (solid lines, blue for O3ctrl and red for O3sen) derived from 100 ensemble members.

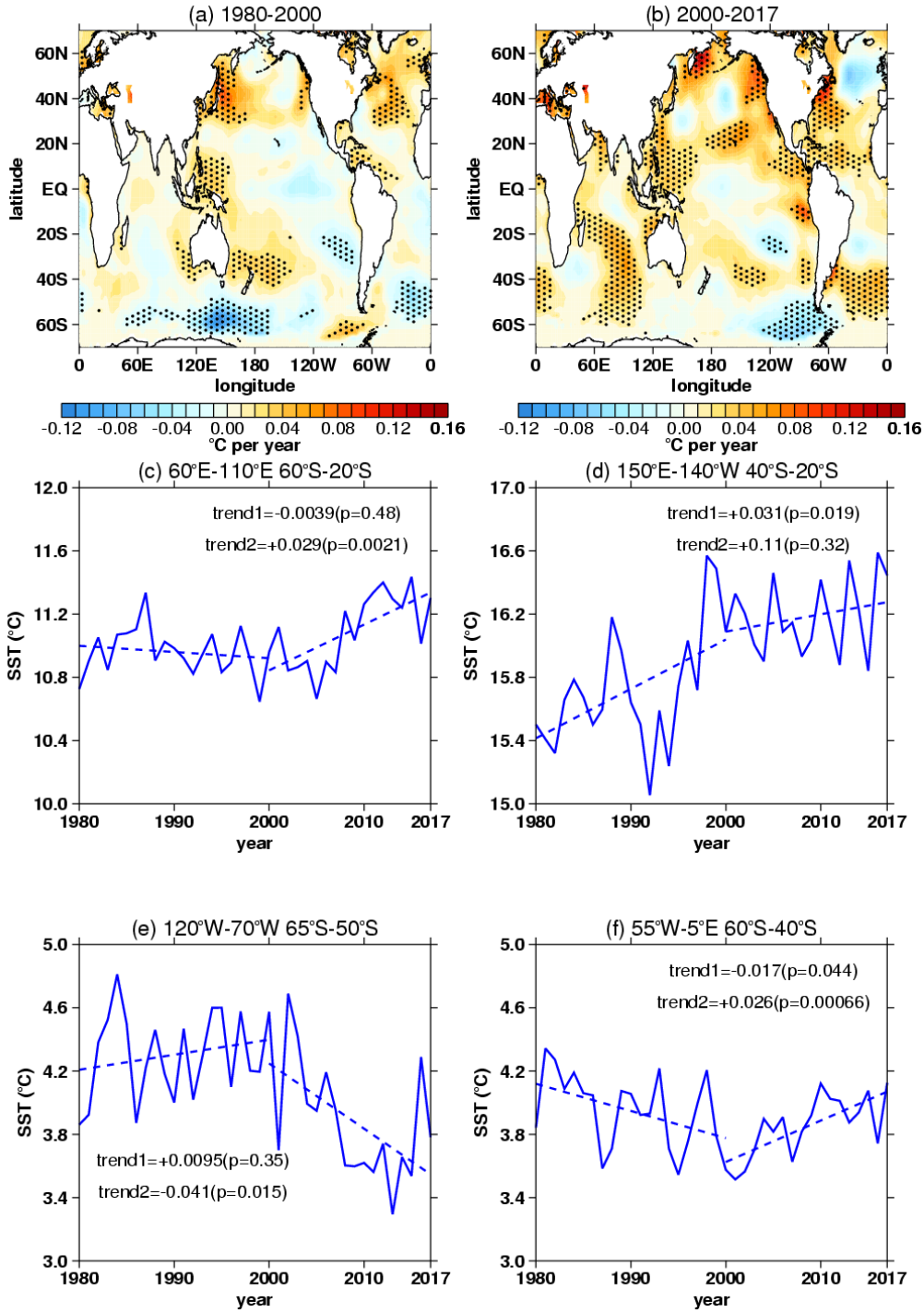

FIG. 8. Trends of SST in September over (a) 1980-2000 and (b) 2000-2017 derived

from ERSST v5 dataset. The stippled regions represent the trends significant at/above the 90% confidence level. (c-f) Time series (blue solid lines) of SST during 1980-2017 over different regions (titles). The dashed lines represent linear regressions of SST time series on piecewise periods (1980-2000 and 2000-2017). The "trend1" and "trend2" labeled in Figs. 8c-f represent the trend coefficients and the corresponding significances (bracketed) over 1980-2000 and 2000-2017, respectively.

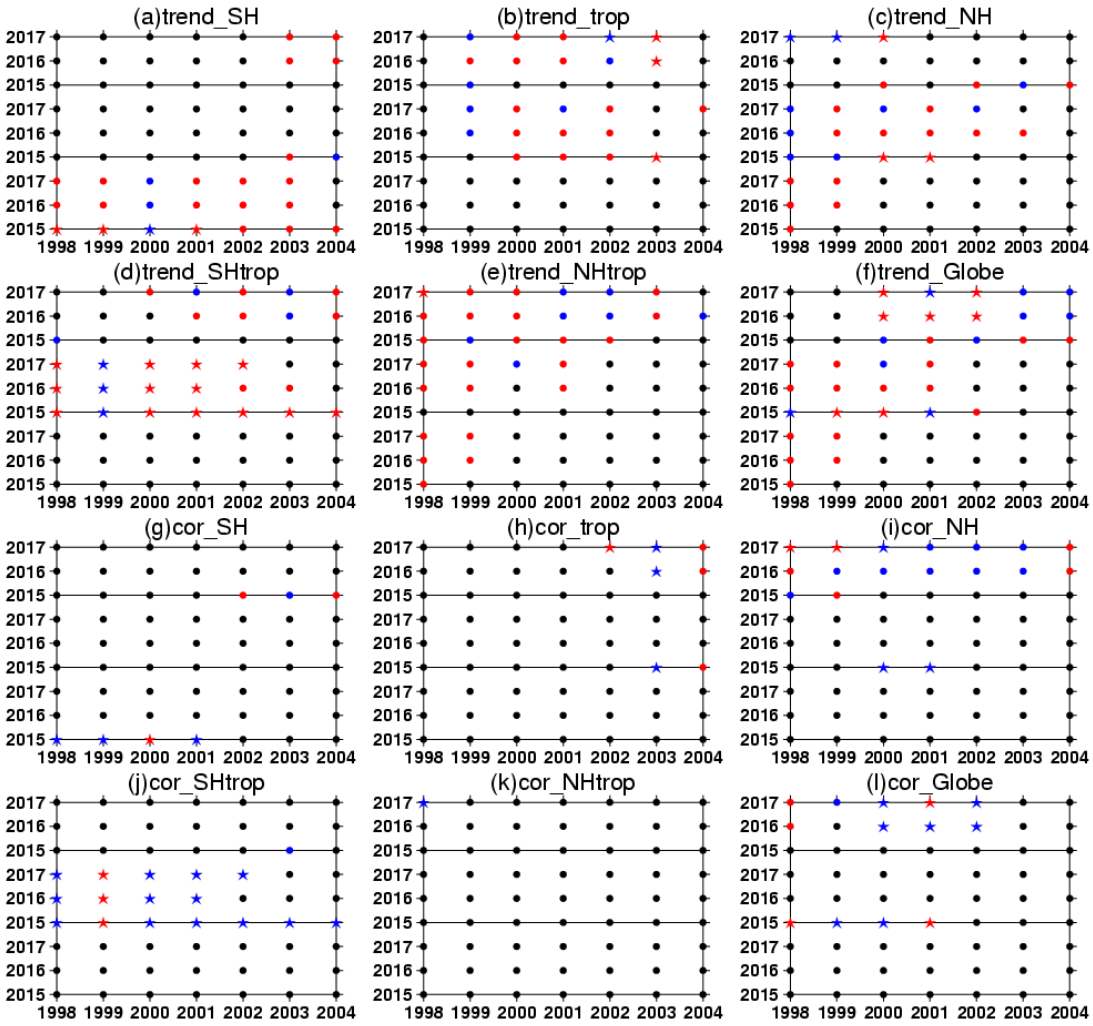

FIG. 9. Trend significance of the first three SST principal components (PCs) in (a) the extratropical southern hemisphere (SH, 70°S-20°S), (b) the tropics (TROP, 20°S-20°N), (c) the extratropical northern hemisphere (NH, 20°N-70°N), (d) the extratropical southern hemisphere and the tropics (SHtrop, 70°S-20°N), (e) the extratropical northern

hemisphere and the tropics (NHtrop, 20°S-70°N), (f) the globe (70°S-70°N) and the corresponding (g, h, i, j, k, l) correlation significances between them and vertical E-P flux (Fz, area-weighted from 100 hPa to 30 hPa over 70°S-50°S) during different beginning years (x-axes) and ending years (y-axes). The red and blue dots indicate positive and negative trend or correlation coefficient are significant, respectively. The black dots indicate the trends or correlation coefficients are not significant. The stars indicate that the trends and the corresponding correlation coefficients are both significant. Each panel is divided into three regions from bottom to top, corresponding to the first, the second and the third principal components, respectively. The criterion to distinguish whether the trends and correlations are significant or not is the 90% confidence level.

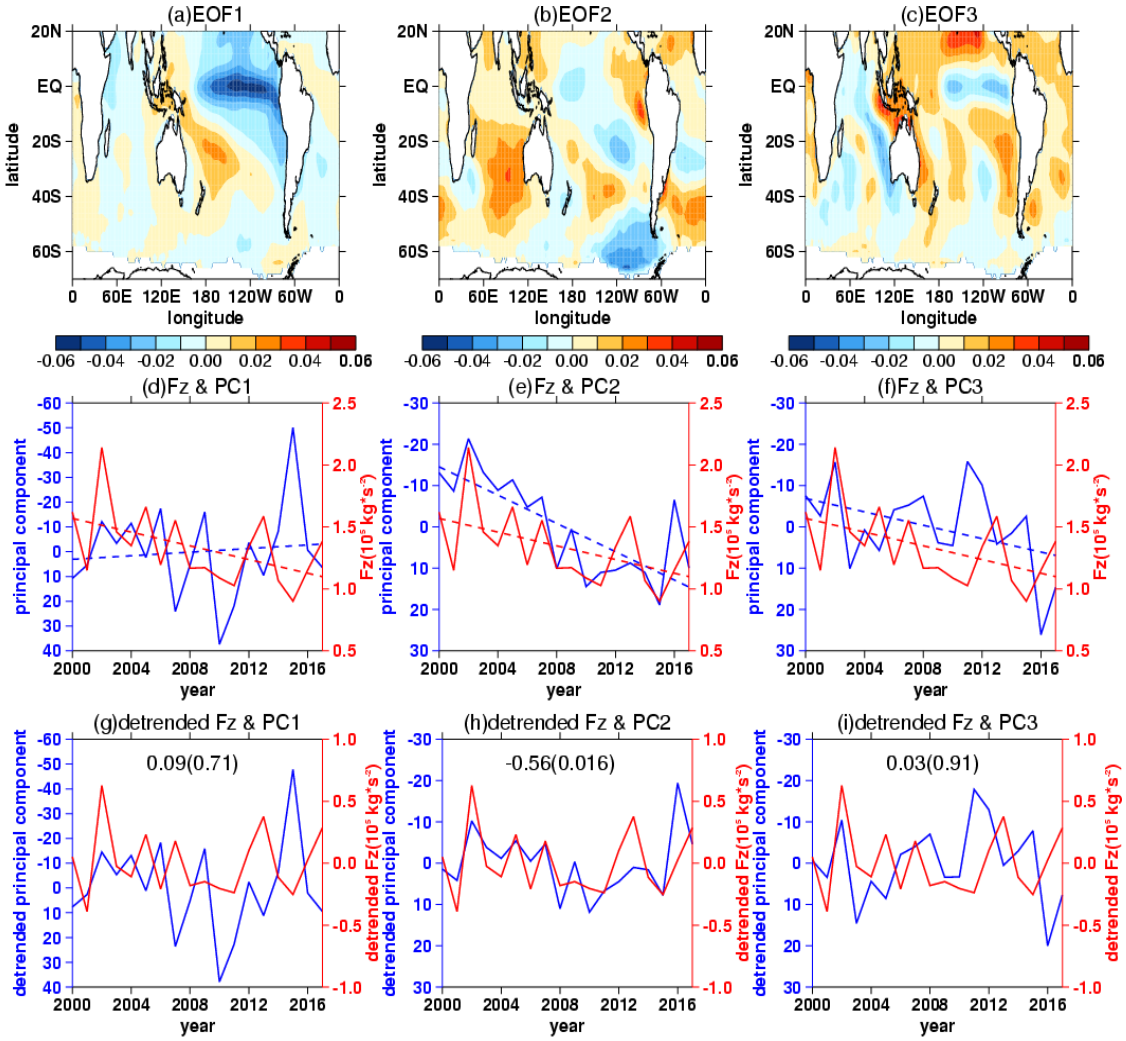

FIG. 10. (a, b, c) The first three EOF patterns of SST in SHtrop region. (d, e, f) The original time series of the first three principle components (PCs, blue solid lines correspond to left inverted y-axes) and stratospheric vertical E-P flux (Fz, area-weighted from 100 hPa to 30 hPa over 70°S-50°S, red solid lines correspond to right y-axes) in September during 2000-2017. The blue and red dashed lines in (d, e, f) represent the linear regressions of PC time series and Fz time series, respectively. The meaning of (g, h, i) are the same as (d, e, f) correspondingly, except the detrended time series. The unbracketed and bracketed numbers in (g, h, i) represent the correlation coefficients between detrended PC time series and Fz time series and the corresponding p values calculated by two-tailed t test, respectively.

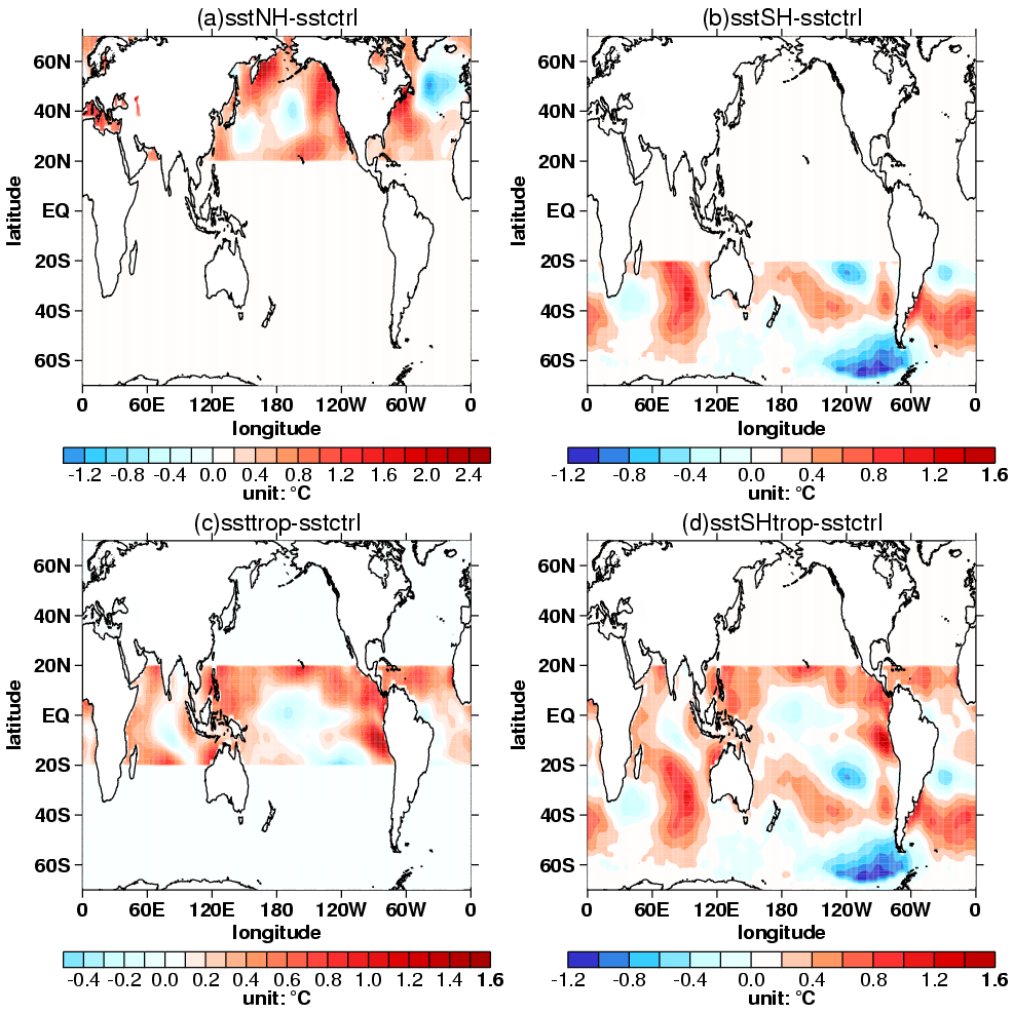

1052

1053 **FIG. 11.** Differences in SST forcing field between sensitive experiments ((a) sstNH; (b)

1054 sstSH; (c) ssttrop; (d) sstSHtrop) and the control experiment (sstctrl).

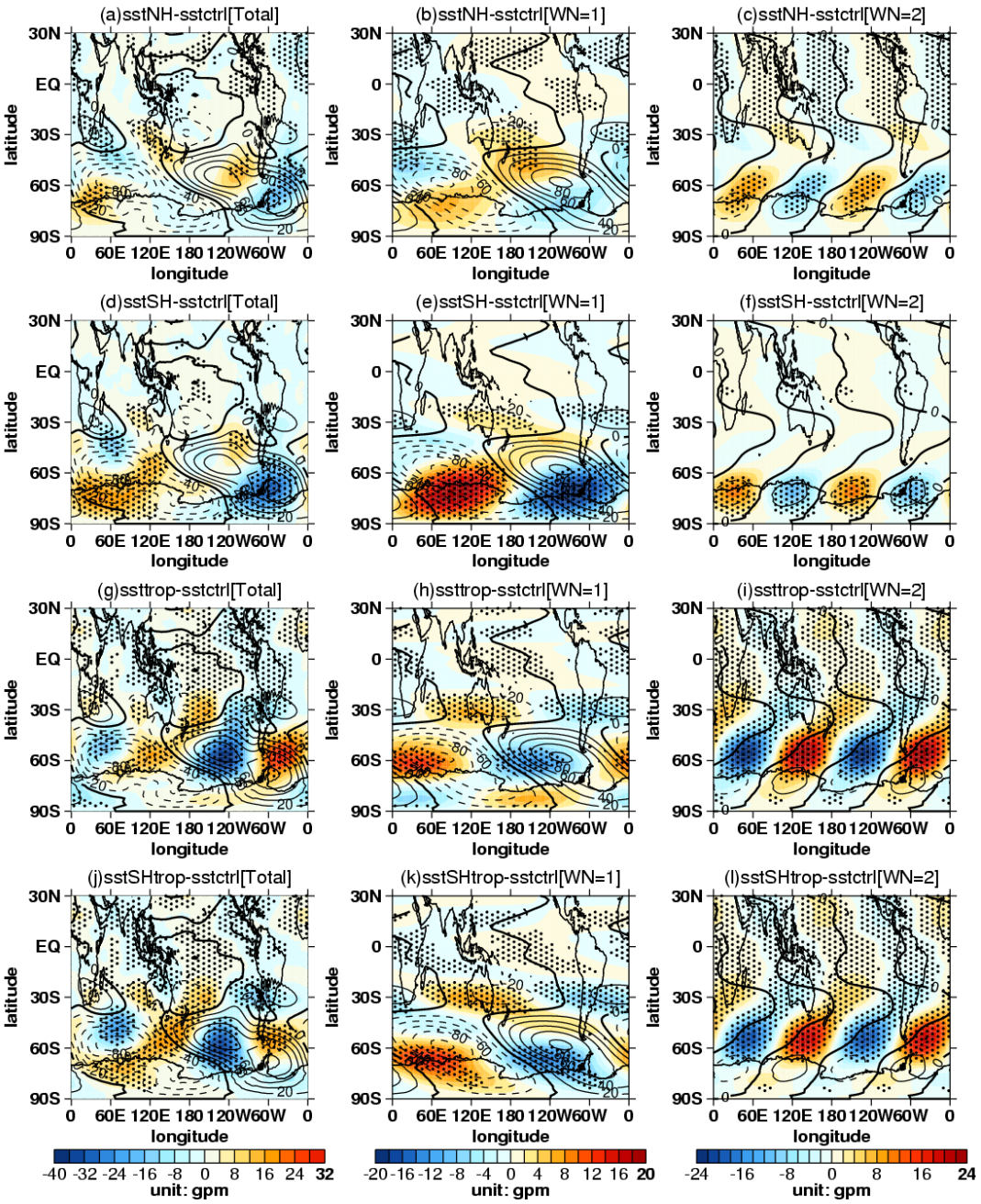

FIG. 12. Differences (shadings) of (a, d, g, j) 500 hPa geopotential height zonal deviations with their (b, e, h, k) wave-1 component and (c, f, i, l) wave-2 component between sensitive experiments ((a, b, c) sstNH; (d, e, f) sstSH; (g, h, i) ssttrop; (j, k, l) sstSHtrop) and the control experiment (sstctrl). The mean distributions (contours with an interval of 20 gpm, positive and negative values are depicted by solid and dashed lines respectively, zeroes are depicted by thick solid lines) of them are derived from the

control experiment. The stippled regions represent the mean difference significant at/above the 90% confidence level.

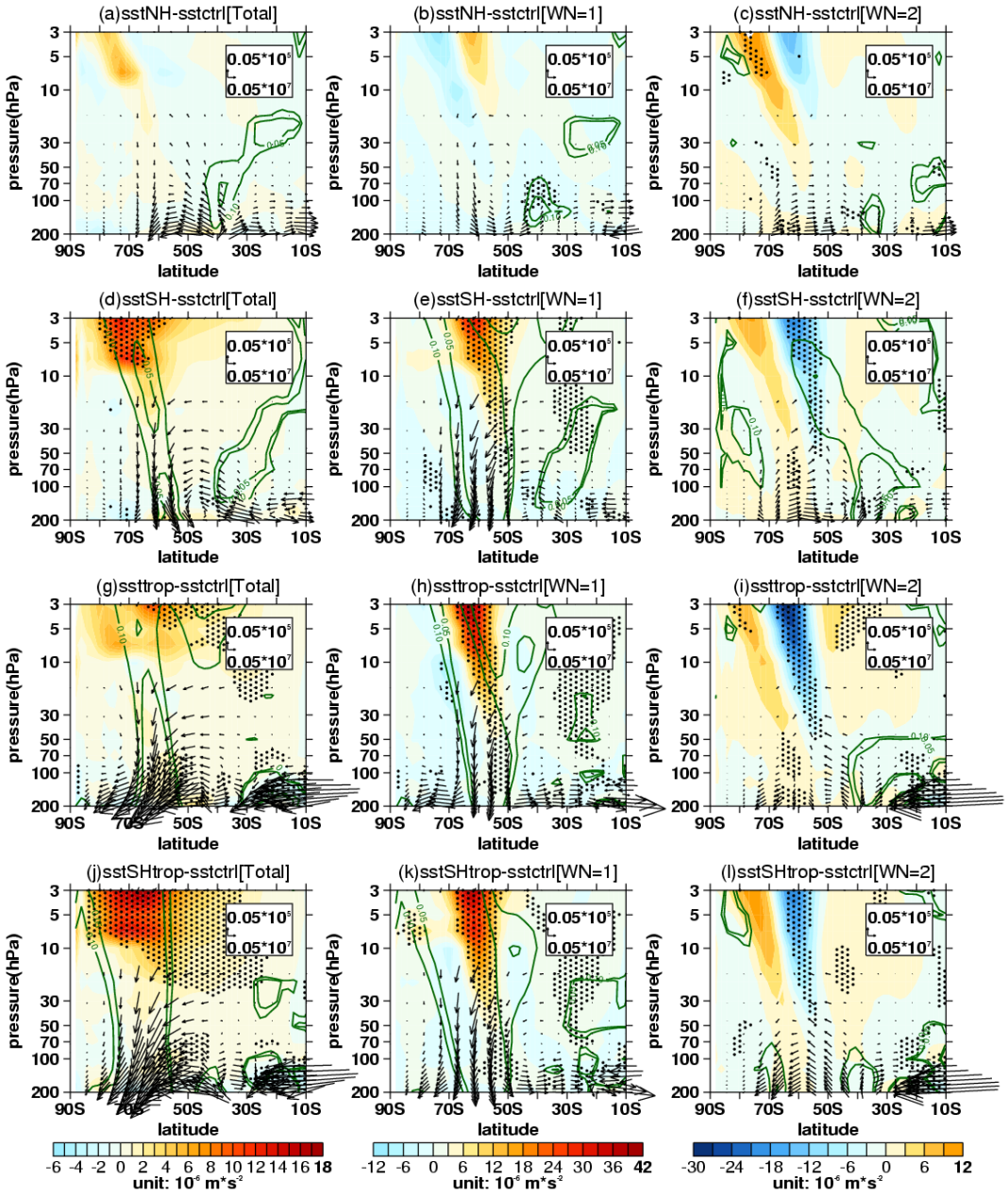

FIG. 13. Differences of (a, d, g, j) stratospheric E-P flux (arrows, units in horizontal and vertical components are 0.05×10^7 and 0.05×10^5 kg·s^{-2}, respectively) and its divergence (shadings) with their (b, e, h, k) wave-1 component and (c, f, i, l) wave-2 component between sensitive experiments ((a, b, c) sstNH; (d, e, f) sstSH; (g, h, i) ssttrop; (j, k, l) sstSHtrop) and the control experiment (sstctrl). The stippled regions

represent the mean differences of E-P flux divergence significant at/above the 90% confidence level. The green contours from outside to inside (corresponding to p=0.1, 0.05) represent the mean differences of vertical E-P flux significant at the 90% and 95% confidence levels, respectively.

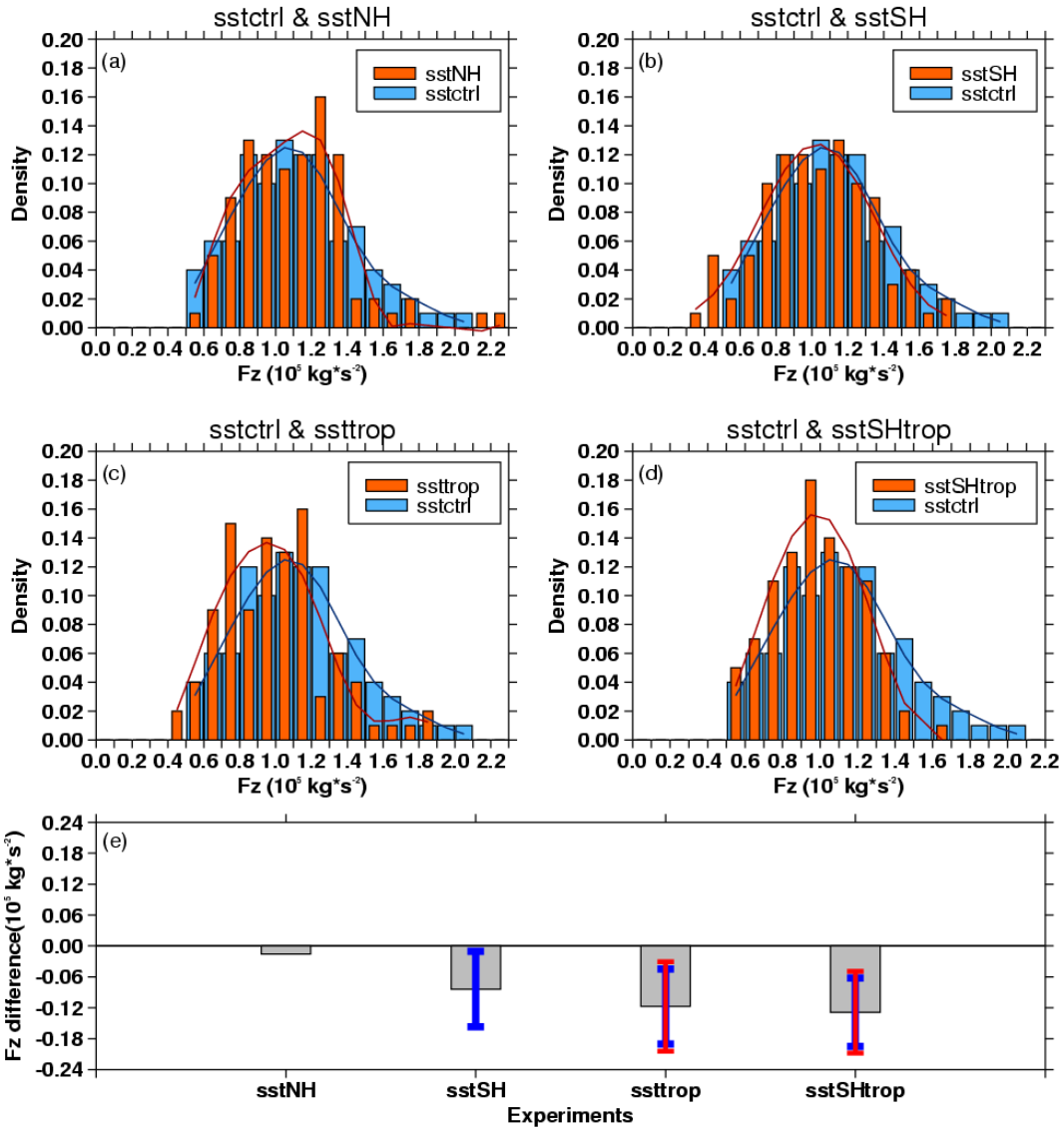

FIG. 14. (a, b, c, d) Frequency distributions (pillars, blue for control experiment and orange for sensitive experiments) of vertical E-P flux (Fz, area-weighted from 200 hPa to 10 hPa over 70°S-50°S) and its 5-point low-pass filtered fitting curves (solid lines, blue for control experiment and red for sensitive experiments) derived from 100

ensemble members of the control experiment (sstctrl) and sensitive experiments ((a) sstNH; (b) sstSH; (c) ssttrop; (d) sstSHtrop), respectively. (e) Mean differences (grey pillars) and corresponding uncertainties (error bars) of Fz between sensitive experiments and the control experiment. The blue and red error bars reflect the 90% and 95% confidence levels calculated by two-tailed t test, respectively. The error bar is omitted when the significance of mean difference is lower than the corresponding confidence level.

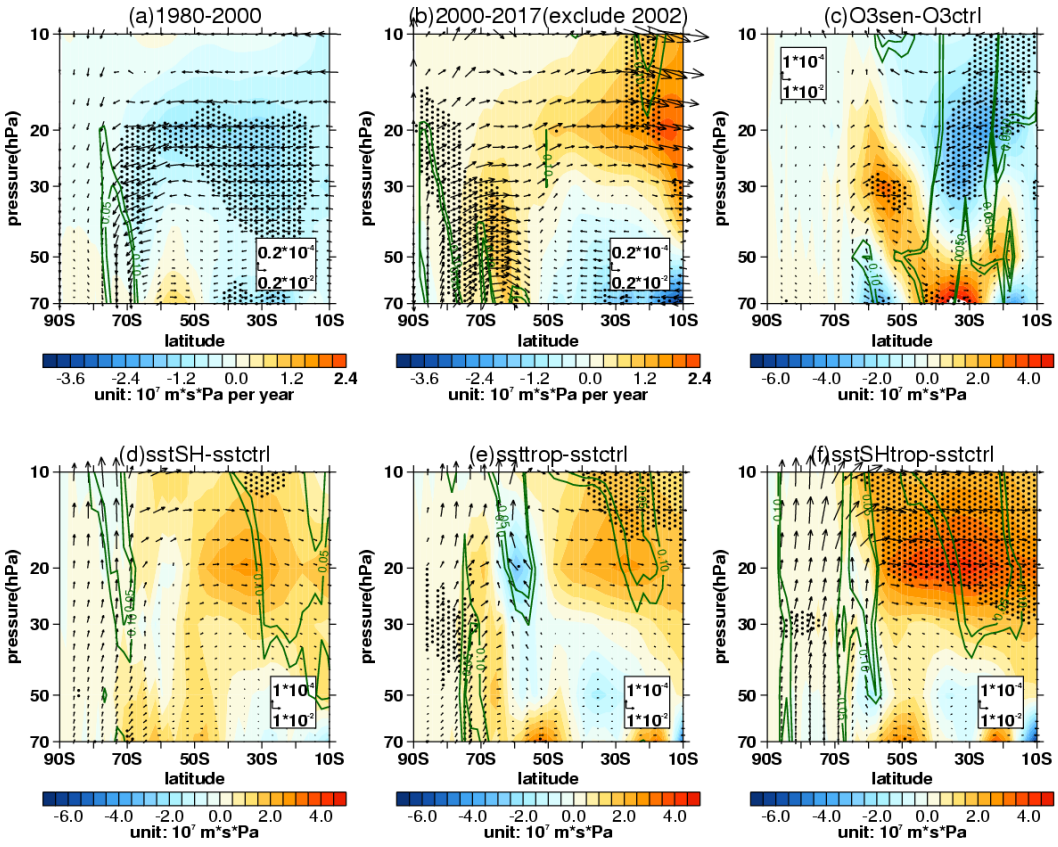

FIG. 15. (a) Trends of southern hemispheric Brewer-Dobson circulation (arrows, units in horizontal and vertical components are 0.2×10^{-2} and 0.2×10^{-4} $m\cdot s^{-1}$ per year, respectively) and its stream function (shadings) in September during (a) 1980-2000 and (b) 2000-2017 derived from MERRA-2 dataset. Data in 2002 are removed when trends

are calculated in Figure (b). (c) Differences of Brewer-Dobson circulation (arrows, units in horizontal and vertical components are 10^{-2} and 10^{-4} $m \cdot s^{-1}$, respectively) and its stream function (shadings) between the O3ctrl and O3sen. (d, e, f) Differences of Brewer-Dobson circulation and its stream function between the control experiment (sstctrl) and sensitive experiments ((d) sstSH; (e) ssttrop; (f) sstSHtrop) with SST changes. The stippled regions represent the trends or differences of the stream function significant at/above the 90% confidence level. The green contours from outside to inside (corresponding to p=0.1, 0.05) represent the trends or differences of the vertical components significant at the 90% and 95% confidence levels, respectively.